ARCHIVIO ISTITUZIONALE
DELLA RICERCA

Alma Mater Studiorum Università di Bologna
Archivio istituzionale della ricerca

Aerodynamic overshoot of rectangular cylinders under accelerating inflow conditions

This is the final peer-reviewed author's accepted manuscript (postprint) of the following publication:

Published Version:
Li, W., Yao, Y., Zhao, L., Chen, C., Patruno, L. (2025). Aerodynamic overshoot of rectangular cylinders under accelerating inflow conditions. PHYSICS OF FLUIDS, 37(6), 1-19 [10.1063/5.0272163].

Availability:
This version is available at: https://hdl.handle.net/11585/1037256 since: 2026-01-15

Published:
DOI: http://doi.org/10.1063/5.0272163

Terms of use:

Some rights reserved. The terms and conditions for the reuse of this version of the manuscript are specified in the publishing policy. For all terms of use and more information see the publisher's website.

This item was downloaded from IRIS Università di Bologna (https://cris.unibo.it/).
When citing, please refer to the published version.

(Article begins on next page)

15 October 2026

Aerodynamic overshoot of rectangular cylinders under accelerating inflow conditions

Weilin Li[a,b] (李威霖), Yunkai Yao[a,b] (姚云开), Lin Zhao[a,b*] (赵林) , Cong Chen[a,b] (陈聪), Luca Patruno[c]

[a] *State Key Laboratory of Featured Metal Materials and Life-cycle Safety for Composite Structures (Provincially and Ministerially Co-constructed), Nanning Guangxi 530004, China*

[b] *School of Civil Engineering and Architecture, Guangxi University, Nanning Guangxi 530004, China*

[c] *DICAM, University of Bologna, Viale Risorgimento 2, 40136 Bologna, Italy*

* *Correspondence: zhaolin-gxu@gxu.edu.cn*

Abstracts: The overshoot phenomenon, where aerodynamic coefficients of bluff sections under accelerating flows exceed those in steady flows, is critical and controversial issue in the study of non-synoptic wind effects. Experimental simulation of accelerating flows requires complex dedicated facilities, which makes the investigation of key acceleration parameters affecting the aerodynamic overshoot still a challenging task. Therefore, numerical methods that allow easy control of acceleration parameters are urgently needed. In this study, aiming at verifying the accuracy of existing force evaluation approaches, we consider four types of accelerating inflows, namely, *Linear*, *Hyperbolic*, *Sinusoidal*, and *Turbulent*. The unsteady aerodynamic forces of rectangular cylinders with aspect ratios ranging from 3 to 16 are investigated using Unsteady Reynolds-averaged Navier-Stokes and Large Eddy Simulations. Sixteen different accelerating cases are considered to examine the effects of dimensionless acceleration parameters (a_p) that defined by flow acceleration relative to velocity and deck height. Results show that accelerating flows cause drag overshoots well described by Morison equation, but reduce vortex-induced lift forces. The a_p is the key parameter governing drag overshoot, as it increases the absolute values of windward positive and leeward negative pressures. Additionally, the added mass coefficients are identified and an empirical formula is proposed to accurately estimate drag overshoot. The study provides guidance for the numerical simulation and drag estimation for bluff sections impinged by non-synoptic winds.

Key words: Accelerating inflows; Rectangular cylinders; Overshoot; Aerodynamic loads; Computational Fluid dynamics (CFD)；

1. Introduction

With global climate change, more frequent strong typhoons, thunderstorms, and downbursts, non-synoptic winds become a significant challenge in wind-resistant safety for infrastructure [1-3]. In fact, such non-synoptic winds can show maximum speeds which can exceed 75 m/s [4] and exhibit rapid acceleration, leading to significant wind-induced vibrations [5, 6] and damage [7] on slender structures. Current analysis methods for non-stationary wind-induced vibrations are well-established [8-13], but generally assume that aerodynamic coefficients are independent from the flow acceleration and rely on results obtained under stationary flow conditions [9]. However, if overshoots of the aerodynamic forces occur due to the flow acceleration, existing wind-resistant design approaches may result in unsafe predictions. Therefore, investigating the aerodynamic overshoot of bluff sections in accelerating flows is essential for non-synoptic wind designs.

Whether aerodynamic coefficients in accelerating flows exhibit overshoot phenomena remains controversial in current studies. Early water tunnel research by Sarpkaya et al. [14-17] defined the overshoot coefficient as the ratio between the aerodynamic coefficients in accelerating flow and that in steady conditions, and found that the overshoot coefficients for circular and rectangular cylinders were 1.35 and 1.62, respectively. Takeuchi et al. [18] conducted active wind tunnel tests (WTTs) and found that overshoot coefficients of elliptical cylinder reach a maximum value of 5. Dong et al. [19] found that the drag, lift, and moment coefficients of a bluff girder increased by approximately 1.1, 1.5, and 1.35 times, respectively, compared to steady flows. They emphasized the importance of considering such amplification in the wind-resistant design of large-span bridges. Yan et al. [20] investigated the pressure coefficients of a wind turbine nacelle using multi-bladed actively controlled WTTs, and found that wind pressure overshooting occurs on the top surface and increases with flow acceleration. However, many scholars have reported opposite conclusions, where aerodynamic coefficients under accelerating flows are lower than those under steady flows. For instance, Li et al. [21] investigated the aerodynamic effects of a 5:1 rectangular cylinder under downburst-strike flows using multi-fan actively controlled WTTs, and found that static lift coefficient is lower than in

stationary flows. Yang et al. [22] conducted WTTs on rectangular cylinders with aspect ratios of 1/3, 1, and 3 at angle of attack of 0° and found that acceleration flows did not lead to larger wind loads compared to steady cases. Le et al. [23] conducted active WTTs of the scaled Commonwealth Aeronautical Advisory Research Council (CAARC) building model and found that aerodynamic coefficients under non-stationary inflows decrease to approximately 70% of those under steady inflows. Brusco et al. [24] conducted multiple-fan WTTs and found that drag coefficients of a square cylinder at 0° angle of attack are lower than that in accelerating flows, except for a small overshoot of 1.8% at the start and the end of the ramp-down case. Moreover, the root mean square (RMS) of lift coefficients decreases as the acceleration increases, and the vortex-shedding frequency show constant-frequency time cells phenomenon. Chen et.al [25] conducted multi-fan WTTs of a 3:2 rectangular section and found that drag coefficients under accelerating flows are consistent with the quasi-steady value. In a summary, existing literature shows contradictory findings regarding the intensity of the overshoots in the aerodynamic coefficients when accelerating flows are considered.

Another unresolved issue is the lack of clarity regarding the key parameters affecting the overshoots with respect to the quasi-static values. The dimensionless acceleration parameters a_p ($D(dU/dt)/U^2$) is known to be an important factor affecting the aerodynamic forces of bluff sections during accelerating flows [14, 22, 26]. However, the heterogeneous definition of acceleration parameters a_p within the available sources adds to the uncertainty of overshoot, with sometimes using the time-varying velocity [24] and others relying on the start speeds a_{ps} ($D(dU/dt)/U_s^2$) [14] or end speeds a_{pe} ($D(dU/dt)/U_e^2$) [22]. For instance, Takeuchi et al. [18] observed the overshoot coefficient is increasing linear as a_p within the range of 0.43 to 5.11. In contrast, Brusco et al. [24] found no apparent trend between the drag forces of a square cylinder and a_p within the range of 0.001 to 0.008. Sarpkaya et al. [14] introduced a_{ps} to account for the initial history of flow acceleration and found that it strongly affects the overshoot when ap below 1, but has limited effects on drag and lift forces for $1< a_{ps} <2.5$. They further pointed out that a systematic variation of a_p using WTTs is extremely difficult and the best one can hope for is to maintain it as constant and as large as possible. Therefore, the relationship between

acceleration parameters a_p and aerodynamic overshoot remains debated. Regarding the effects of incoming turbulence, non-synoptic winds are inherently turbulent and can be regarded as a superposition of a time-varying mean velocity with zero-mean fluctuating turbulent fluctuations [27-29]. Full-scale measurements [27, 30] of non-synoptic wind events found that the ensemble mean value of turbulence intensity is in the order of 11% to 34%. It is well-known that free-stream turbulence significantly affects the flow separation of bluff sections, so potentially affecting the intensity of the overshoots. However, research on the effect of turbulence in accelerating flows is limited, due to the challenges of controlling turbulence properties in WTTs while dealing with accelerating inflows. Briefly, available facilities for such studies can be subdivided into impinging jet simulators [31], such as the WindEEE [32-34], multi-fan wind tunnel [19, 35, 36], and active-controlled multi-blade device [20, 23, 37]. Despite the remarkable advancements made by using such dedicated infrastructures [38-41], challenges remain in investigating accelerating inflows using WTTs, especially as achieving high a_p requires rapid wind speed increase that may exceeds the capabilities.

A possible alternative to WTTs is represented by Computational Fluid Dynamics (CFD) simulations [42-49], which has become an important tool for studying aerodynamic forces of bluff sections [50, 51]. Guo et al. [52] performed Large Eddy Simulations (LES) to investigate the flow field evolution and its aerodynamic characteristics of a square cylinder in accelerating inflows. Lunghi et al. [53] investigated a square cylinder under Gaussian-type accelerating inflows with a_p range of 0.0076~0.0151 and found no overshoot in aerodynamic coefficients. Takeuchi et al. [54] conducted LES of a square building under short-duration gusts and found significant overshoot in pressures and displacements compared to steady cases. Xing et al. [55] conducted LES of a large sports stadium and found that non-stationary inflows could amplify wind loads when the rump-up time is in the order of 30 s. Xue et. al utilized an improved Delayed Detached Eddy Simulation (DDES) and observed a significant overshoot in aerodynamic loads acting on the train during short-rise gusts. However, CFD studies focus on the aerodynamic overshoot of bluff sections under accelerating flows remain very limited.

In this paper, Unsteady Reynolds-averaged Navier-Stokes (URANS) and LES simulations are adopted to investigate the aerodynamic coefficient overshoot with respect to quasi-static theory for rectangular cylinders with different aspect ratios. The accuracy of present simulations is verified by comparison with accelerating inflows WTTs [22, 56]. First, we focus on a rectangular cylinder with aspect ratio 4 and use three types of accelerating inflows *Linear*, *Hyperbolic*, *Sinusoidal* characterized by different acceleration speeds, durations and non-dimensional parameters a_p. This approach allows us to maintain a constant a_p or a_{ps} to examine their effect on the aerodynamic overshoot. Given the large number of considered acceleration cases, URANS-based simulations are adopted aiming to identify the key parameters determining the overshoot. Next, *Sinusoidal*-type accelerating inflows with three-dimensional turbulence synthesized using Prescribed-wavevector Random Flow Generator (PRFG^3) [45] and LES are adopted to clarify the effects of turbulence. Finally, rectangular cylinders with aspect ratios ranging from 3 to 16 under the same *Sinusoidal*-type accelerating inflow are adopted to investigate the effect of aspect ratio. The added mass coefficients due to flow acceleration are identified and an empirical equation is proposed to accurately account for drag overshoot, aiming to establish a relationship between accelerating inflows and steady cases.

This paper is organized as follows: Section 2 introduces the Morison theory and the synthetic generation of four types of accelerating inflows. Section 3 briefly presents active WTTs setup to validate the subsequent CFD simulations. Section 4 describes the URANS and LES settings. Section 5 discusses the results, and finally conclusions are drawn in Section 6.

2. Aerodynamic forces and synthetic generation of accelerating inflows

2.1 Morison equation and non-dimensional acceleration parameters

The aerodynamic forces acting on a fixed body in an accelerating flow can be described by the Morison equation [57-59]. Such equation represents the force as the sum of two components: a drag force proportional to the square of the instantaneous velocity $U(t)$, and an inertia force in phase with the local flow acceleration $\dot{U}(t)$, as below:

$$F_D(\mathrm{t}) = \frac{1}{2}\rho U(\mathrm{t})^2 D\bar{C}_D + \rho A C_a \dot{U}(t) = \frac{1}{2}\rho U(\mathrm{t})^2 D\left(\bar{C}_D + 2C_a RD\frac{\dot{U}(t)}{U(\mathrm{t})^2}\right), \quad (1)$$

where ρ is the flow density, B and D is the immersed body characteristic width and depth, respectively. A=B×D is the reference area, R=B/D is the aspect ratio, C_a is the added mass coefficient, and $\bar{C}_D$ is the drag coefficient obtained in stationary flows. The non-dimensional acceleration parameter a_p is defined as [14, 24]:

$$a_p = D\frac{\dot{U}(t)}{U(\mathrm{t})^2}. \quad (2)$$

Substituting Equation (2) into Equation (1), the time-varying drag coefficient under accelerating flows can be obtained as:

$$C_D(\mathrm{t}) = \frac{2F_D(\mathrm{t})}{\rho U(\mathrm{t})^2 D} = \bar{C}_D + 2C_a R a_p. \quad (3)$$

Equation (3) establishes a relationship between the aerodynamic coefficients under stationary and non-stationary conditions, with the added mass coefficient C_a as parameter to be identified. In order to simplify the formulation above for practical purposes, an acceleration parameter a_{ps}, made non-dimensional using the speed at the start of the accelerating phase, U_s, has been adopted by many scholars [22, 52]:

$$a_{ps} = D\frac{\dot{U}(t)}{U_s^2}. \quad (4)$$

It worth noting that although Morison theory has been widely adopted to calculate the hydrodynamic forces on slender cylinders under accelerating wave [60, 61], its applicability to the aerodynamic characteristics of bluff sections under accelerating winds is worth being revisited, especially for immersed bodies presenting flow separations and reattachments.

2.2 Accelerating inflows

To clarify the effects of the different definition of the acceleration parameters on aerodynamic forces (i.e. a_p and a_{ps}), the following four types of synthetic accelerating inflows are adopted. The first is the *Linear*-type accelerating inflow [52], characterized by a constant

non-dimensional parameter a_{ps}, while the parameter a_p changes continuously with the acceleration time. The theoretical expression for the *Linear*-type accelerating inflow is:

$$U(t)=\frac{U_s^2 a_{ps}}{D}(t-t_s)+U_s \quad \left(t_s \le t \le t_e\right), \tag{5}$$

where t_s and t_e represents the acceleration start and end time, respectively, and $\Delta T=t_e-t_s$ denotes the acceleration duration time. The second is the *Hyperbolic*-type accelerating inflow, characterized by a constant non-dimensional acceleration parameter a_p while a_{ps} changes over time. The expression for the *Hyperbolic*-type acceleration inflows is defined as:

$$U(t)=\frac{-DU_s}{a_p U_s t-a_p U_s t_s-D} \quad \left(t_s \le t \le t_e\right). \tag{6}$$

It is noteworthy that the above accelerating inflows do not satisfy the conditions for continuous differentiability at the acceleration start and end positions, which is inconsistent with the accelerating flows simulated in WTTs [18, 35]. To better match WTTs, the third *Sinusoidal*-type accelerating inflows, characterized by time-varying non-dimensional acceleration parameter a_p and a_{ps}. The theoretical expression is given as follows:

$$U(t)=\frac{U_e+U_s}{2}+\frac{U_e-U_s}{2}\cos\left(\frac{t-t_s}{t_e-t_s}\pi\right) \quad \left(t_s \le t \le t_e\right), \tag{7}$$

where U_e represents the acceleration end speed. Aiming at investigating the effects of incoming turbulence superimposed to the accelerating flow, the fourth *Turbulent*-type accelerating inflows is considered. Three-dimensional turbulence is generated using the synthetic spectra method PRFG^3 [45] and can be described as follows [62]:

$$\mathbf{u}(\mathbf{x},t)=\sum_{n=1}^{N}\left[\mathbf{p}^n\cos(\mathbf{k}^{nT}\mathbf{x}+\omega^n t)+\mathbf{q}^n\sin(\mathbf{k}^{nT}\mathbf{x}+\omega^n t)\right], \tag{8}$$

where $\mathbf{u}=[u,v,w]^T$ is the fluctuating wind components vector, $x=\left[x,y,z\right]$ denotes the three-dimensional coordinate vector, t is time, N is the number of sampled wavevectors, $\boldsymbol{p}^n$ and $\boldsymbol{q}^n$ are random amplitude vectors, $\boldsymbol{k}^n$ is a vectorial wavenumber, ω^n is a circular frequency and $(\cdot)^T$ denotes the transposition operator. Then, the time-varying mean wind speed using Eq. (7) is

superimposed to generate accelerating inflows with three-dimensional turbulent components, as detailed below:

$$\mathbf{U}(\mathbf{x},t) = (U(t),0,0) + \mathbf{u}(\mathbf{x},t) = \left(\frac{U_e + U_s}{2} + \frac{U_e - U_s}{2}\cos\left(\frac{t - t_s}{t_e - t_s}\pi\right),0,0\right) + \sum_{n=1}^{N}\left[\mathbf{p}^n \cos(\mathbf{k}^{nT}\mathbf{x} + \omega^n t) + \mathbf{q}^n \sin(\mathbf{k}^{nT}\mathbf{x} + \omega^n t)\right], \quad (9)$$

Based on the above mentioned four types of accelerating inflows, the acceleration parameters including acceleration types, start and end speeds, duration time, as well as non-dimensional parameters a_p and a_{ps}, can be easily controlled.

3. Active wind tunnel tests

This section provides a brief overview of the active WTTs setup [56], which serve as validation data for numerical simulations. Figure 1(a) shows the TJ-5 multi-fan wind tunnel at Tongji University, featuring a cross-section size of 1.5 m (width) × 1.8 m (height) and a total length of 10 m. Such facility is capable of simulating various accelerating inflows [19, 21, 35, 36, 63, 64]. Figure 1(b) shows the rigid rectangular cylinder model with aspect ratio of 5:1, measuring 0.3 m (B)× 0.06 m (D) and a length of 1.2 m. [56]. Wind speed is measured using a three-components Cobra probe, and reference pressure is obtained with a Pitot tube. A total of 250 pressure tapes are arranged along 5 sections of the rectangular cross-section model to measure the non-stationary aerodynamic forces. To avoid discrepancies caused by synchronized measurements of wind speed and aerodynamic force, the instantaneous drag and pressure coefficients are normalized by the acceleration end speeds:

$$C_{D,e}(t) = \frac{2F_D(t)}{\rho U_e^2 D},\ C_{p,s}(t) = \frac{2(p(t) - p_\infty)}{\rho U_e^2}, \quad (10)$$

where p (t) is the instantaneous pressure, and p_∞ is the static pressure.

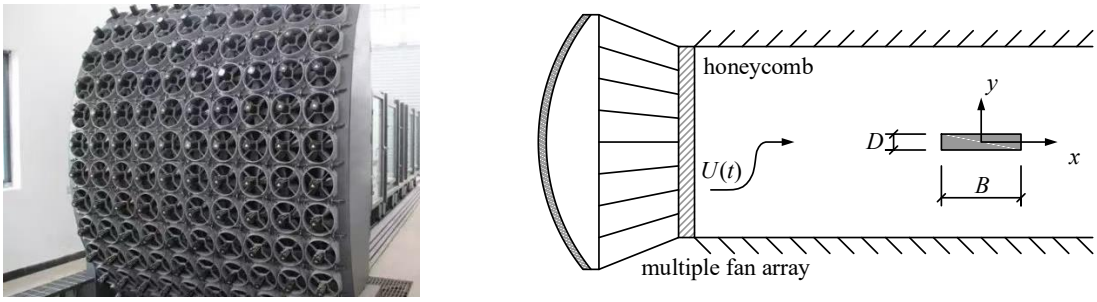

(a) (b)

Figure 1. Active WTT setup: (a) multi-fan array; (b) schematic of rectangular cylinder in accelerating flows [56].

4. Numerical setup and validation

4.1 Target accelerating inflow conditions

Table. 1 provides the parameters for the four types of considered accelerating inflows. The non-dimensional acceleration parameter a_p is within the range 0.002 to 0.05, which is close to the measured values for typhoons and downbursts [6, 57, 65-68]. In particular, for *Linear*-type inflows (*L*-1, *L*-2 and *L*-3), the acceleration speeds are the same while shortening the acceleration duration results in a_{ps} values of 0.009, 0.018, and 0.036, respectively. For *L*-4, only a_{ps} is the same as *L*-3, but the start, end speed and duration are different. Similarly, for *Hyperbolic*-type inflows (*H*-1, *H*-2 and *H*-3), the acceleration speeds are the same while shortening the acceleration duration adjusts a_p to 0.009, 0.018, and 0.036, respectively. For *H*-4, only the non-dimensional parameters a_p is same as *H*-3 but other parameters are different. For the *Sinusoidal*-type inflows (*S*-1, *S*-2 and *S*-3), both a_p and a_{ps} vary over time. By adjusting end speed and duration, the maximum a_p values of *H-i*, *L-i* and *S-i* (*i*=1, 2, 3) are consistent. These setups allow the effects of acceleration, start speed, end speeds, as well as non-dimensional acceleration parameters a_p and a_{ps} to be separately investigated.

Table. 1 Parameter settings for the four types of accelerating inflows numerical simulations

Case	U_s (m/s)	U_e (m/s)	ΔT (s)	B/D	a_p	a_{ps}
L-1	3.0($\bar{U}$)	5.0	6.1728	4	0.003-0.009	0.009
L-2	3.0	5.0	3.0864	4	0.006-0.018	0.018
L-3	3.0	5.0	1.5408	4	0.013-0.036	0.036
L-4	3.5	7.0	1.9830	4	0.009-0.036	0.036

H-1	3.0	5.28	4.0	4	0.009	0.009-0.028
H-2	3.0	5.28	2.0	4	0.018	0.018-0.056
H-3	3.0	5.28	1.0	4	0.036	0.036-0.112
H-4	3.5	7.06	1.0	4	0.036	0.036-0.146
S-1	3.0	6.0	8.0	4	0-0.009	0-0.016
S-2	3.0	6.0	4.0	4	0-0.018	0-0.033
S-3	3.0	6.0	2.0	3、4、5、8、10、12、16	0-0.036	0-0.065
S-WT-1 [56]	6.2	10.5	2.0	5	0-0.0033	0-0.0053
S-WT-2 [22]	2.3	25.8	3.0	3	0-0.028	0-0.0011
S-3+5%*Tu*	3.0	6.0	2.0	4	0-0.036	0-0.065
S-3+10%*Tu*	3.0	6.0	2.0	4	0-0.036	0-0.065
S-3+15%*Tu*	3.0	6.0	2.0	4	0-0.036	0-0.065

Furthermore, the aforementioned cases mainly focus on the rectangular cylinder with aspect ratio 4 (denoted as *R*4), while cases *R*3, *R*5, *R*8, *R*10, *R*12, and *R*16 under *S*-3 inflow are used to investigate the effects of aspect ratio and validate the Morison equation. In addition, two *Sinusoidal*-type inflows, *S-WT*-1 and *S-WT*-2, correspond to the WTTs in literatures [22, 56] are used to validate the CFD results. Finally, *Turbulent*-type accelerating inflows, based on *S*-3 with added synthetic turbulence intensity 5%, 10% and 15%, and turbulence integral scale of 0.34*B*, are adopted to investigate the effects of turbulence.

4.2 Domain, mesh and numerical settings

2D URANS with *k*-*ω* SST turbulence model are adopted for rectangular cylinders with *Linear*, *Hyperbolic* and *Sinusoidal*-type accelerating inflows without synthetic turbulent components, while 3D LES with One-Equation turbulence model is used for *R*4 under *Turbulent*-type accelerating inflows. These two turbulence models are well-established in the literature for the CFD simulation of bluff sections[69-73].

Figure 2 shows the computational domain followed the guidelines of BARC project for the 5:1 rectangular cylinder [74], with the domain dimensions are $15B(x) \times 10B(y)$ and a maximum vertical blockage ratio of 2.9%. The computational mesh consists of four different refinement regions. The finest mesh near the rectangular cylinder is structured and the size is approximately $0.0049B(x) \times 0.0009B(y)$, while the mesh size gradually increases in the other

three regions. The total number for 2D URANS is 180k cells, while 3D LES with a spanwise length of 1.5B and 20 layers in the extrusion directions uses about 3.6M cells, meeting the spanwise requirements of LES [75, 76]. An overview of the meshes adopted near the cylinders is provided in Figure 3.

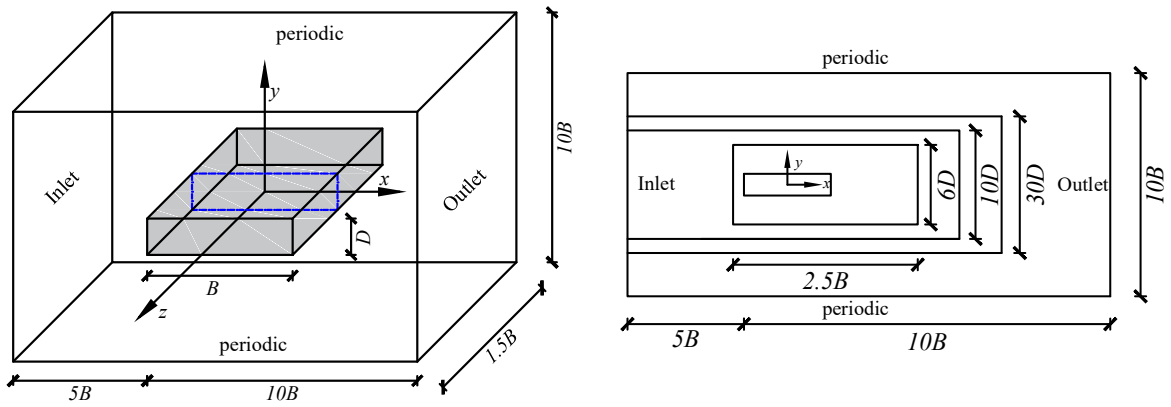

(a) (b)

Figure 2. Numerical model: (a) computational domain; (b) mesh zones (the figure does not respect real proportions).

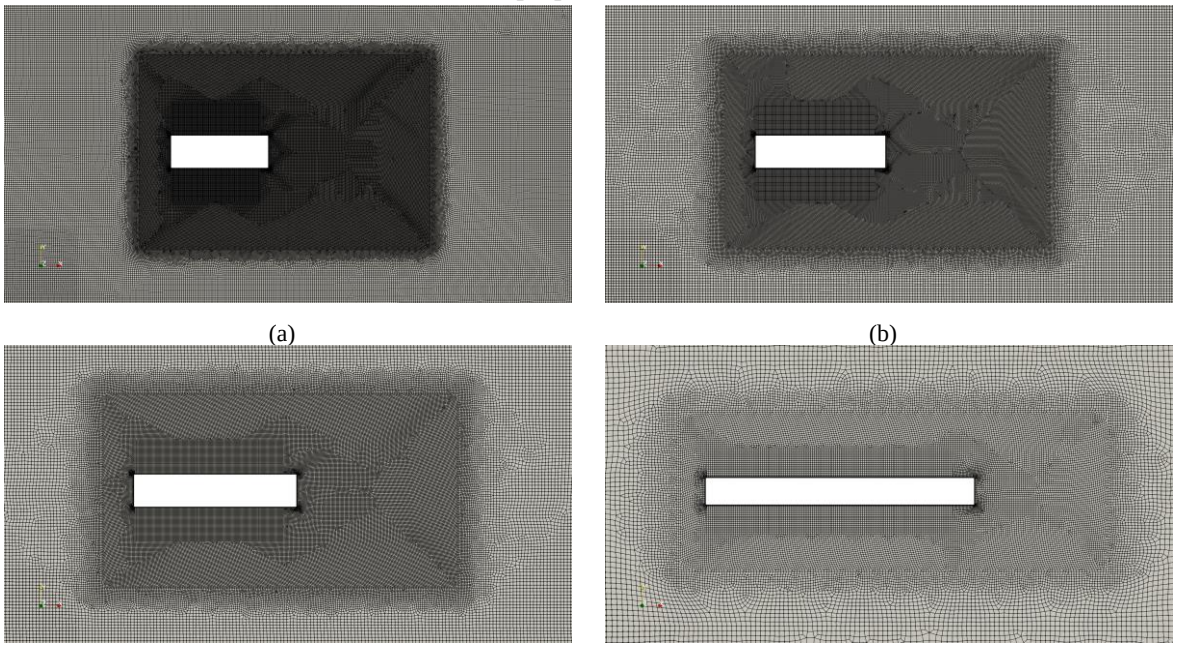

(a) (b)

(c) (d)

Figure 3. Detailed meshes around rectangular cylinders: (a) $R3$; (b) $R4$; (c) $R5$; (d) $R10$.

Regarding the numerical schemes, a centered second-order accurate scheme is employed to discretize the diffusion terms, while a linear upwind scheme is selected for solving the convection terms. Time integration is performed using a transient second-order Crank-Nicolson scheme, while Pressure-velocity coupling using the transient PISO algorithm. Regarding the boundary conditions, a time-varying Dirichlet condition is applied at the inlet to

impose synthetic accelerating inflows, while a Neumann condition is imposed on the pressure field. At the outlet, a null-pressure boundary condition is applied and an inlet-outlet boundary condition for velocity. Periodic boundary conditions are used on top, bottom and sides surfaces.

The maximum Courant number are between 1.2 to 2.5 for URANS and 1.2 to 2.9 for LES, occurring in a few small cells. The average value of y^+ are below 2.1. All simulations were conducted using OpenFOAM-v2112 on a workstation equipped with AMD EPYC 7763 CPU.

4.3 Validation

Three different meshes, denoted as Coarse, Medium, and Fine, are used for *R*4 to assess mesh independence. The length of the finest mesh δ_x near *R*4 decrease from 6.03×10^{-3} to $2.45\times10^{-3}B$, while the height δ_y decrease from 1.21×10^{-3} to $4.88\times10^{-4}B$. The total number of cells increase from 163.3k to 375.8k. Detailed mesh properties are provided in Table. 2.

Table. 2 Mesh properties of *R*4 for 2D URANS.

Case	δ_x/B	δ_y/B	Boundary layers	Total cells (k)
Coarse	6.03×10^{-3}	1.21×10^{-3}	30	163.3
Medium	4.90×10^{-3}	9.40×10^{-4}	40	180.0
Fine	2.45×10^{-3}	4.88×10^{-4}	80	375.8

Figure 4 shows pressure coefficient distributions for *R*4 under steady inflow for the three considered meshes. A good agreement is observed between the meshes, which also matches well with the experimental data [77]. To balance computational efficiency and accuracy, the medium mesh is used for simulating accelerating inflow cases.

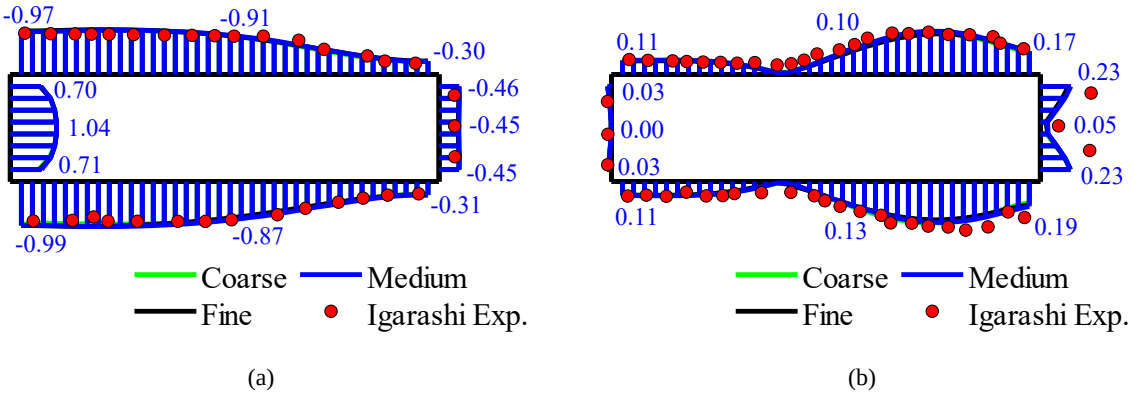

(a) (b)

Figure 4. Pressure coefficients for *R*4 using URANS: (a) time-average; (b) standard deviation.

Table. 3 summarizes aerodynamic coefficients for considered rectangular cylinders. The mean drag coefficient, standard deviation of lift coefficients and Strouhal number show good agreement with the reference data, except for a large deviation for the standard deviation of C_L for $R3$, which is however known to be sensitive to the Reynolds number. Overall, the obtained results confirm the suitability of the adopted model for present investigations.

Table. 3 Summary of aerodynamic coefficients and comparison with results present in the literature. All data calculated with respect to D, except $t-std$ (C_L) and St using B.

Case	Source	Re ($\times 10^4$)	t–avg (C_D)	t–std (C_L)	St
$R3$	Current URANS	1.38~15.48	1.182~1.364	0.1989~0.4059	0.1667~0.1826
	Exp. [22]	0.93-12.3	1.240	0.2900	0.1620
	Exp. [78]	5.16	1.470	0.1400	0.1630
	Exp. [79]	1.30	1.330	-	0.1620
$R4$	Current URANS	7.50	1.246	0.2677	0.1500
	Current LES	7.50	1.108	0.1925	0.1333
	URANS. [80]	2.50	1.227	-	-
	Exp. [77]	6.00	1.213	0.2890	0.1350
	Exp. [81]	7.00	-	0.2370	0.1480
$R5$	Current URANS	7.50	1.109	0.1716	0.1167
	Exp. [82]	2.64	1.029	0.0800	0.1110
	Exp. [83]	5.70	1.042	0.0700	0.1140
	LES. [84]	6.70	1.015	0.0880	0.1120
	Exp. [85]	1.30	1.108	0.0900	0.1110
	URANS. [86]	2.70	1.120	0.1600	0.1120
$R8$	Current URANS	7.50	0.979	0.0255	0.1333
$R10$	Current URANS	7.50	1.066	0.0334	0.1333
	RANS. [87]	1.40	1.040	0.0340	0.1310
$R12$	Current URANS	7.50	1.079	0.0260	0.1333
$R16$	Current URANS	7.50	1.198	0.0310	0.1500

Figure 5 compares the accelerating wind speeds and drag coefficients between CFD and WTTs [56] for $R5$ under S-WT-1 inflows (see in Table. 1). Considering that the abrupt increase in wind speed cause significant changes in the Courant number, a time-step independence study was conducted using $1.5\Delta t$, Δt and $\Delta t/2$ with maximum Courant numbers of 2.08, 1.35, and 0.64, respectively. Results shows that the drag coefficients calculated using Eq. (10) show good

agreement across different time steps and aligns well with the WTTs, with a maximum deviation of less than 12%.

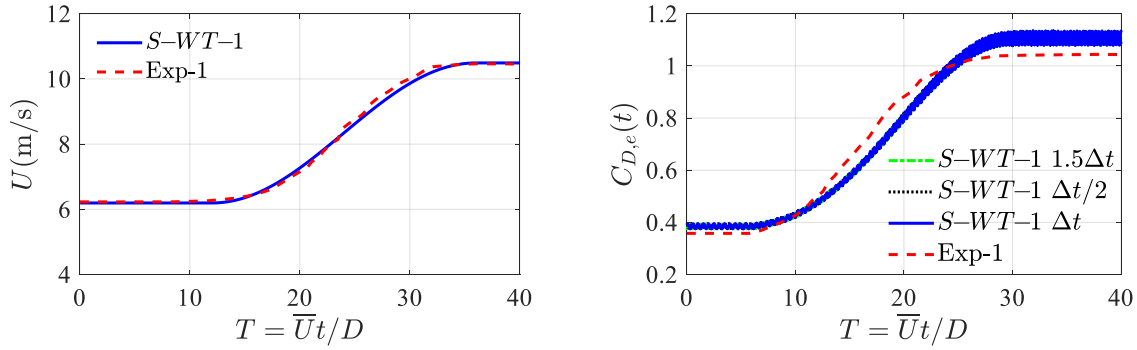

(a) (b)

Figure 5. Time step independence check under *S-WT*-1 conditions: (a) U; (b) $\overline{C}_{D,e}(t)$.

Figure 6 further presents the comparison between the CFD and WTTs [56] in terms of pressure coefficients distribution of *R*5 under *S-WT*-1 during the acceleration phase. Overall, the mean and standard deviation of pressure coefficients obtained from present simulations are in good agreement with the WTTs.

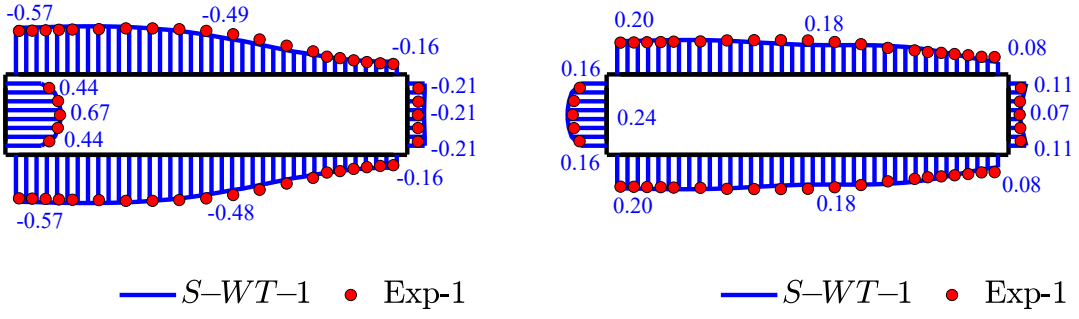

(a) (b)

Figure 6. Pressure coefficients for *R*5 under *S-WT*-1 conditions: (a) time-average; (b) standard deviation.

Figure 7 shows the time-varying speed and drag coefficients of *R*3 under *S-WT*-2 inflows (see Table. 1) between CFD and WTTs [22]. It can be observed that CFD can well reproduce the target acceleration winds and the trend of the corresponding drag coefficients. This indicates that the present CFD setting can effectively simulate the aerodynamic characteristics of the rectangular cylinders under accelerating inflows.

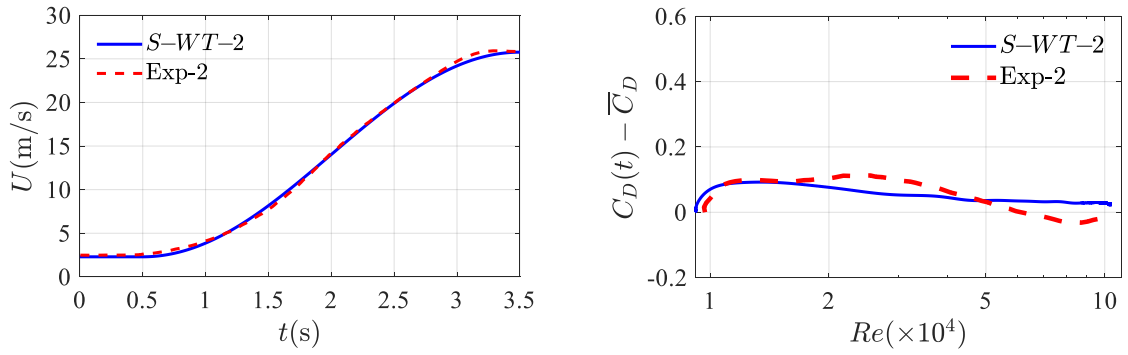

(a) (b)

Figure 7. Time-varying drag coefficients of *R*3 for *a*cceleration case *S-WT*-2: (a) U; (b) $C_D(t)-\overline{C}_D$.

5. Results and discussions

5.1 Accelerating inflows characteristics

Figure 8 shows URANS results for instantaneous velocity, non-dimensional parameter a_p and a_{ps} for the *Linear, Hyperbolic* and *Sinusoidal*-type accelerating inflows. In particular, we remind that a_p is normalized by the instantaneous velocity using Eq. (2), and a_{ps} by the start velocity using Eq. (4). It can be found that CFD results match well with target theoretical values using Eq (5), (6) and (7), respectively. As expected, For *Linear*-type inflow, a_p peaks at the acceleration start point and then ramp down rapidly, while a_{ps} stays constant. For the *Hyperbolic*-type inflow, a_p remains constant while a_{ps} ramp up with acceleration time. For *Sinusoidal*-type inflow, both a_p and a_{ps} first ramp up and then ramp down.

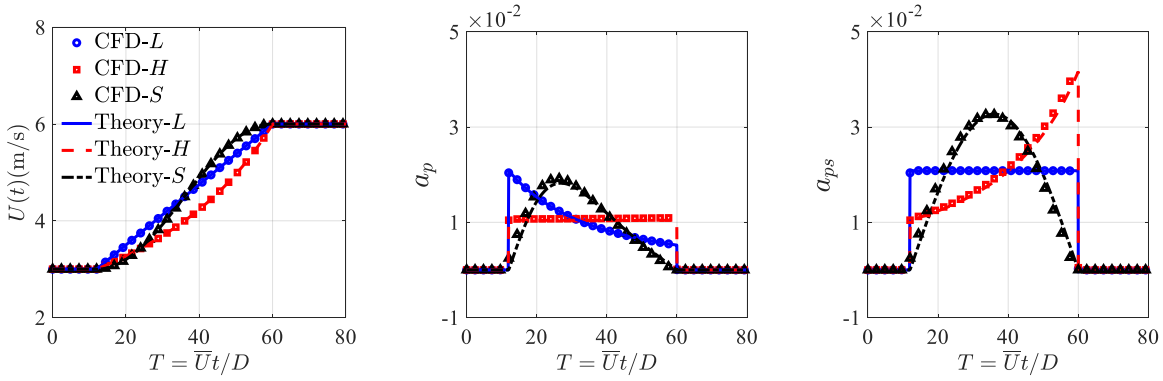

(a) (b) (c)

Figure 8. Comparison of three types of accelerating inflows wind fields: (a) $U(t)$; (b) a_p; (c) a_{ps}.

Coming now to the characterization of *Turbulent*-type accelerating inflow used in conjunction with LES, Figure 9 present the time-history of the accelerating flow, while Figure 10 presents the spectra of fluctuating turbulence components. Results at the inlet, 2.5*B* and 5*B*

from the inlet are in agreement with the target value, indicating that the synthetic turbulence is correctly transported in the LES domain.

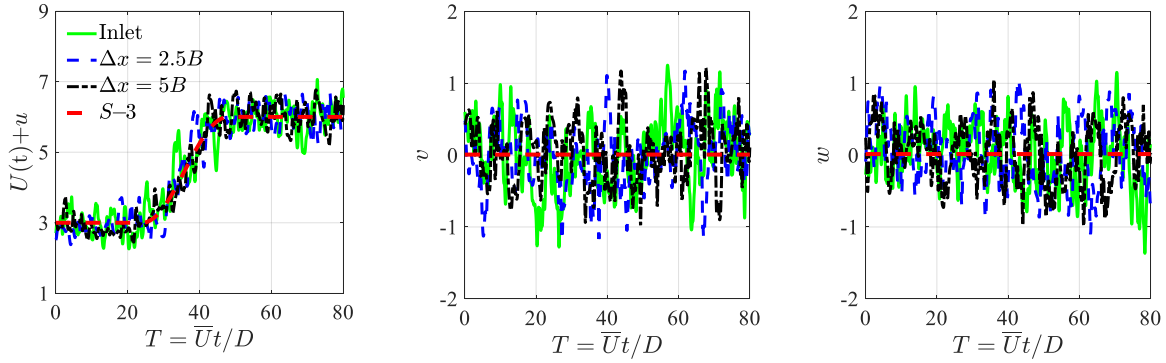

(a) (b) (c)

Figure 9. Time history of wind speed for *Turbulent*-type accelerating inflow: (a) $U(t)+u$; (b) v; (c) w.

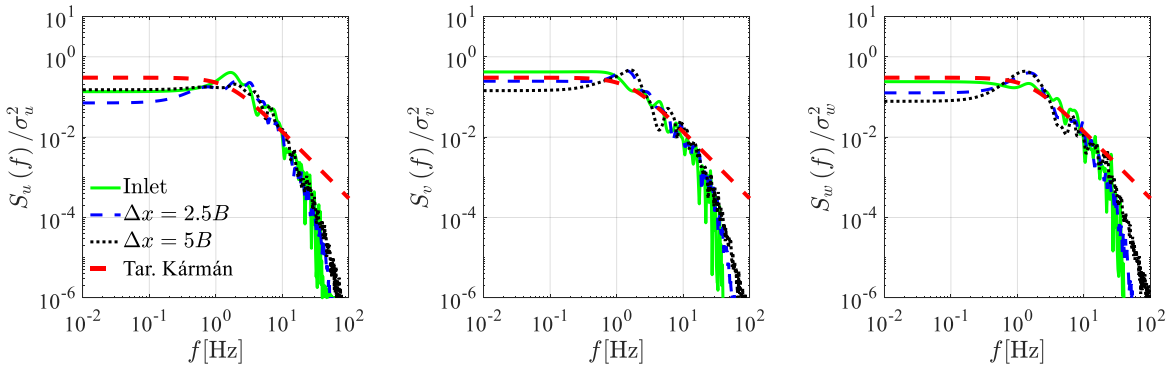

(a) (b) (c)

Figure 10. Spectra of fluctuating components of *Turbulent*-type accelerating inflow: (a) u; (b) v; (c) w.

5.2 Effects of acceleration parameters

Figure 11 provides the drag force for *R*4 under *Linear* and *Hyperbolic*-type accelerating inflows. In particular, the force coefficients are normalized by the instantaneous velocity using Equation (3). For the *Linear*-type inflows shown in Figure 11(a), a_{ps} is constant but a_p ramps down over time. As the a_{ps} increase from 0.009 to 0.036, the drag coefficients exhibit a notable overshoot, with maximum values approximately 6.7%, 14.2%, 28.2% higher than those under steady inflows. Comparing Cases *L*-3 and *L*-4, where have the same a_{ps} and maximum a_p, but different initial and end accelerations, the curve of drag coefficients are found to almost overlap.

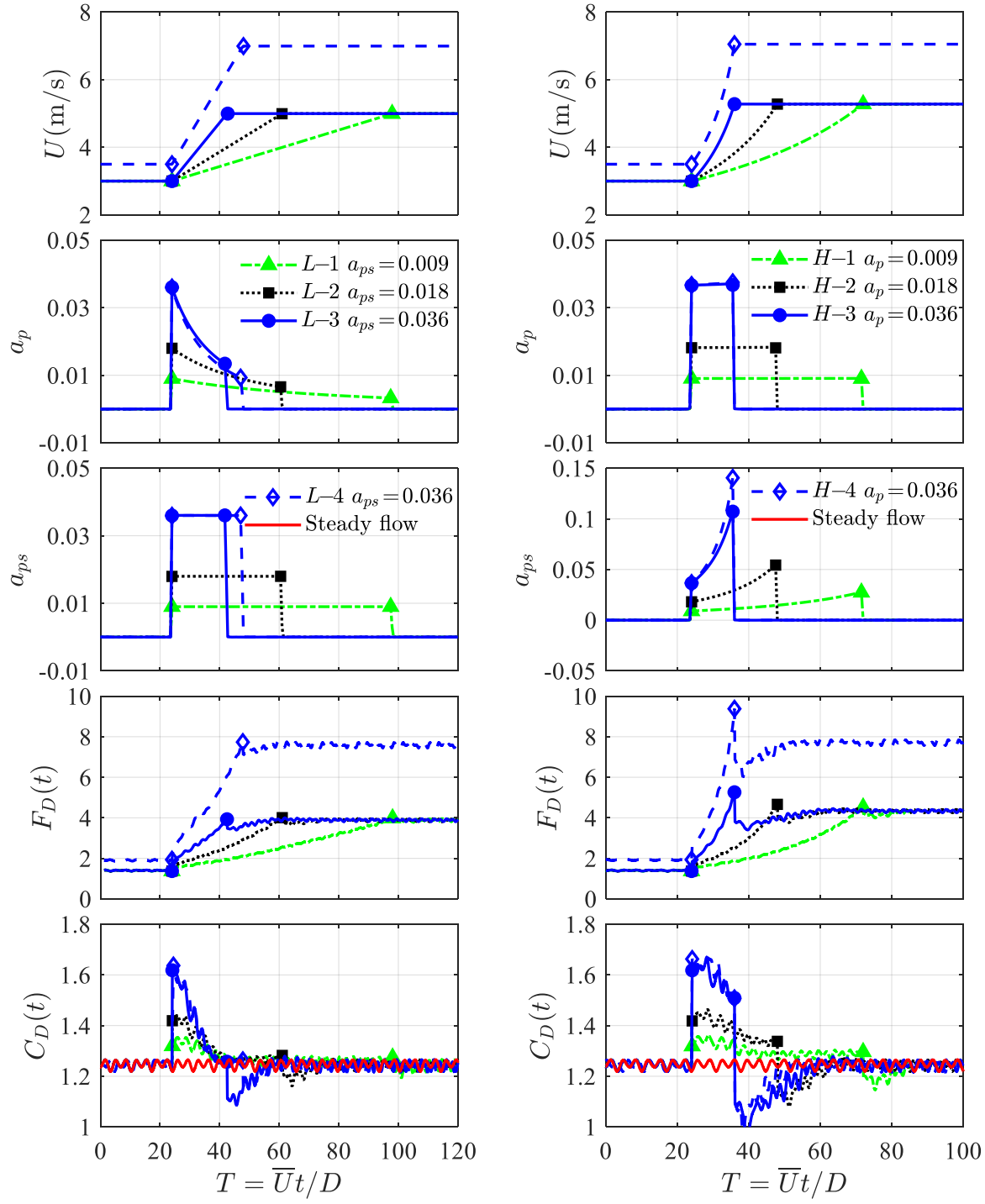

(a) (b)

Figure 11. Drag coefficient of *R*4 for different accelerating flows: (a) *Linear* type; (b) *Hyperbolic* type.

For the *Hyperbolic*-type inflows shown in Figure 11(b), a_p is constant but a_{ps} ramp up over time. It can be found that the drag coefficients exhibit a flat trend, which aligns with a_p but opposes that of a_{ps} during the acceleration phase. Comparing Case *H*-1, *H*-2 and *H*-3, as a_p increases from 0.009 to 0.036 and the maximum a_{ps} rises from 0.028 to 0.112, the maximum

C_D values are approximately 6.7%, 14.5%, 29.4% higher than those under steady inflows. Such results are consistent with those observed in *L*-1, *L*-2 and *L*-3, respectively. Comparing Case *H*-3 and *H*-4, where have the same a_p but different a_{ps}, acceleration start and end speeds, the curve of drag coefficients are almost overlap.

For the *Sinusoidal*-type inflows *S*-1, *S*-2 and *S*-3 shown in Figure 12, a_p first ramps up and then ramps down over time. Comparing Case *S*-1, *S*-2 and *S*-3, as maximum a_p increases from 0.009 to 0.036, the maximum C_D values are approximately similar, 6.4%, 14.0%, 30.4% higher than those under steady inflows. As expected, these increases are consistent with those observed in *Linear* and *Hyperbolic* inflows.

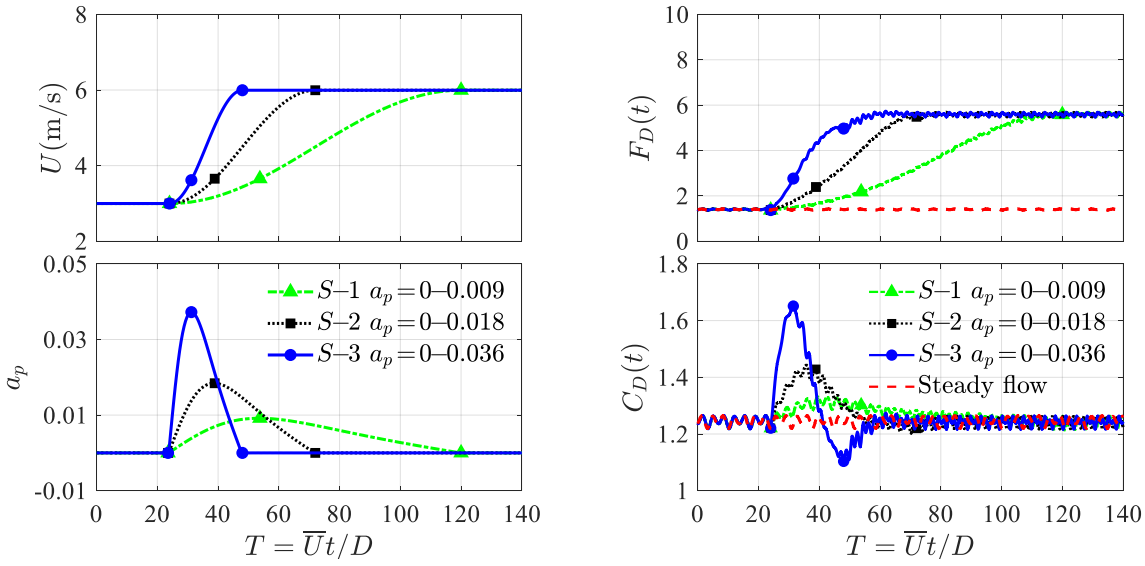

(a) (b)

Figure 12. Drag coefficients of *R*4 for *Sinusoidal*-type accelerating flows: (a) U and a_p; (b) F_D (t) and $C_D(t)$.

Figure 13 further summarizes the drag coefficients obtained by different accelerating flow types, but with the same a_p. It can be found that the maximum drag coefficients are almost the same for different acceleration types. Therefore, the acceleration parameter a_p, made non-dimensional by the instantaneous wind speed, is the most suitable parameter in determining the drag overshoot, with the simplified formulation not always giving comparably accurate results.

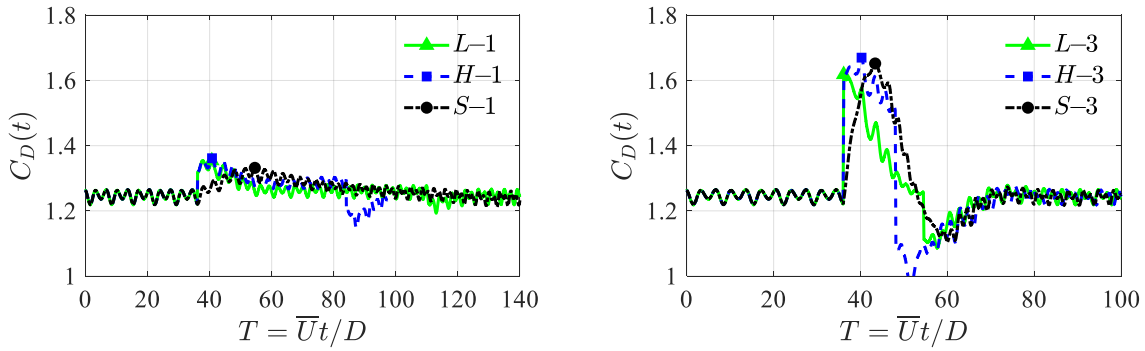

(a) (b)

Figure 13. Drag coefficient of *R*4 under different accelerating flows with $a_{p,max}$ of: (a) 0.009 and (b) 0.036.

Figure 14 clarifies the relationship between instantaneous drag coefficients and the non-dimensional parameters a_p to validate the Morison theory. In particular, Figure 14 (a) shows the results during the a_p ramp-up phase. The drag coefficients for both *Sinusoidal* and *Hyperbolic* type inflows exhibits a linear relation with a_p and are well-described by the Morison theory using Eq.(3) with the added mass coefficient C_a of 1.37. In contrast, Figure 14 (b) shows that during a_p ramp-down phase, the drag coefficients are lower than in the ramp-up phase and influenced by a_p, acceleration duration and inflow type. When a_p drops below 0.01, the drag coefficients fall below the quasi-steady value.

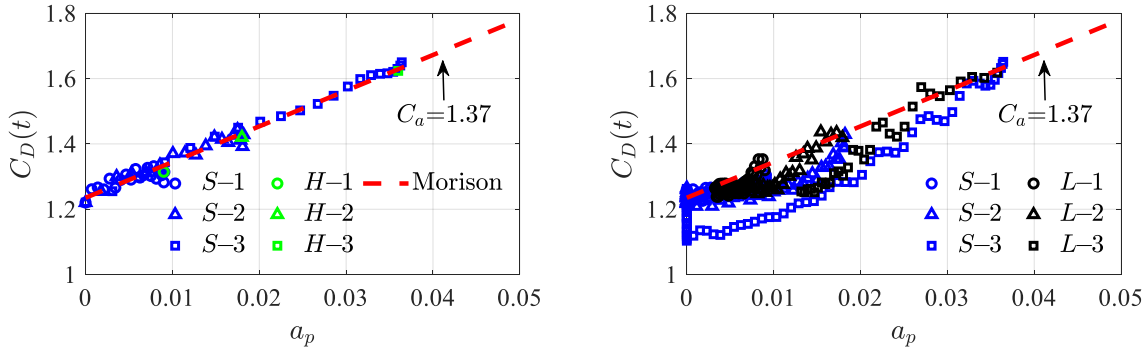

(a) (b)

Figure 14. Instantaneous drag coefficients of *R*4 vs a_p: (a) ramp-up; (b) ramp-down.

In order to explain the mechanism of drag overshoot, the instantaneous pressure coefficients under accelerating inflows are calculated as:

$$C_p(t) = \frac{2(p(t) - p_\infty)}{\rho U(t)^2}. \tag{11}$$

Figure 15 shows mean pressure coefficients $\overline{C}_p$ acting on the vertical windward and leeward sides of *R*4 under *Sinusoidal*-type inflows. For the a_p ramp-up phase shown in Figure

15 (a) and (b), as a_p increase from 0 to 0.036, the positive $\overline{C}_p$ on the windward side increases by approximately 14%, while the negative $\overline{C}_p$ on the leeward side decrease by about 34%. This leads to an increase in the net pressure coefficients and cause drag coefficient overshoot. In contrast, for the a_p ramp-down phase shown in Figure 15 (c) and (d), only $\overline{C}_p$ on the windward side increase while the negative $\overline{C}_p$ on the leeward side remains constant, resulting in a lower overshoot compared to the ramp-up phase.

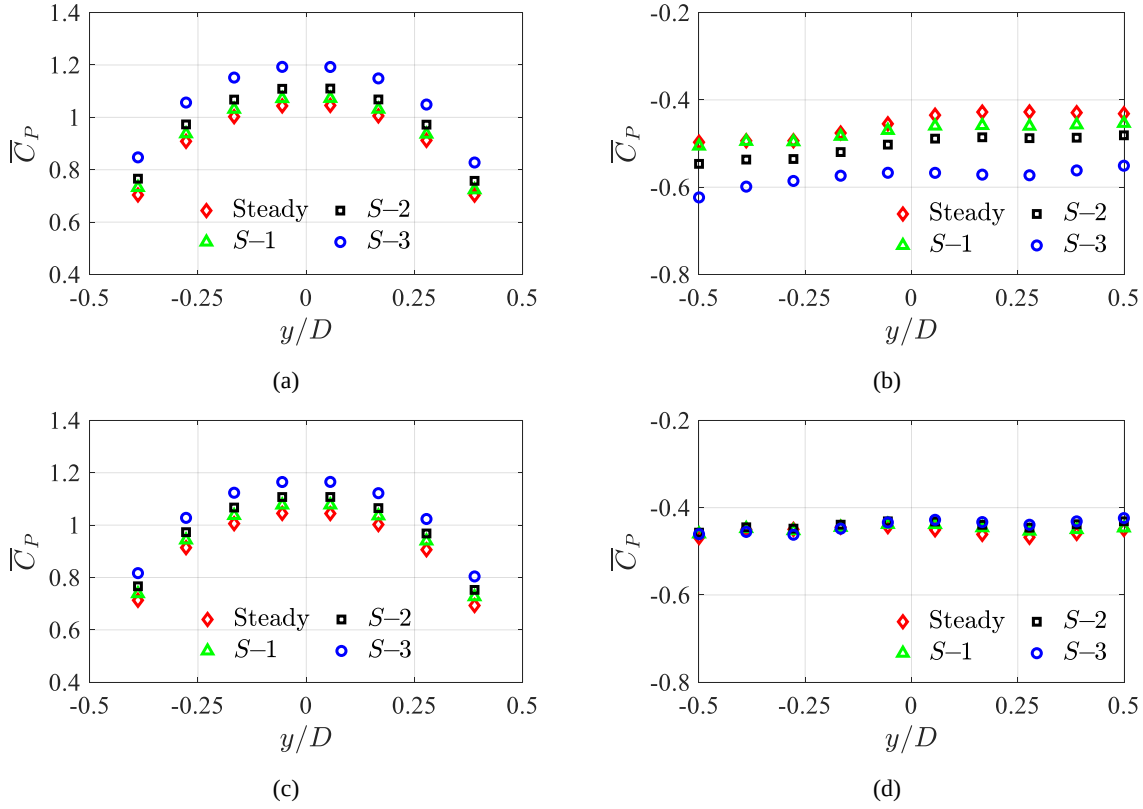

Figure 15. Mean pressure coefficients in *Sinusoidal*-type inflows: (a) and (b) windward and leeward sides during a_p ramp-up; (c) and (d) during a_p ramp-down.

Figure 16 provides the instantaneous pressure flow fields of $R4$ under S-3 condition at different time instants. Comparing Figure 16 (a)~(c), as a_p ramp up from 0 to 0.036, the windward pressure rises from 1.0 to a maximum of 1.3 due to flow acceleration. Meanwhile, the lowest negative pressure in the wake region of Kármán's vortex street drops from -0.8 to -1.1, leading to an increase in net pressure and a drag overshoot. Conversely, as a_p ramps down from 0.036 back to 0 in Figures 16(c)~(f), the windward pressure decreases from 1.3 to 1.0. Furthermore, the lowest negative pressure in the wake region of Kármán's vortex street rises

from -1.1 to -0.3, even exceeding the steady value when a_p returns 0. This results in a reduction of the drag overshoot, eventually causing aerodynamic forces to drop below the quasi-steady values as acceleration comes to an end and a_p approaches 0.

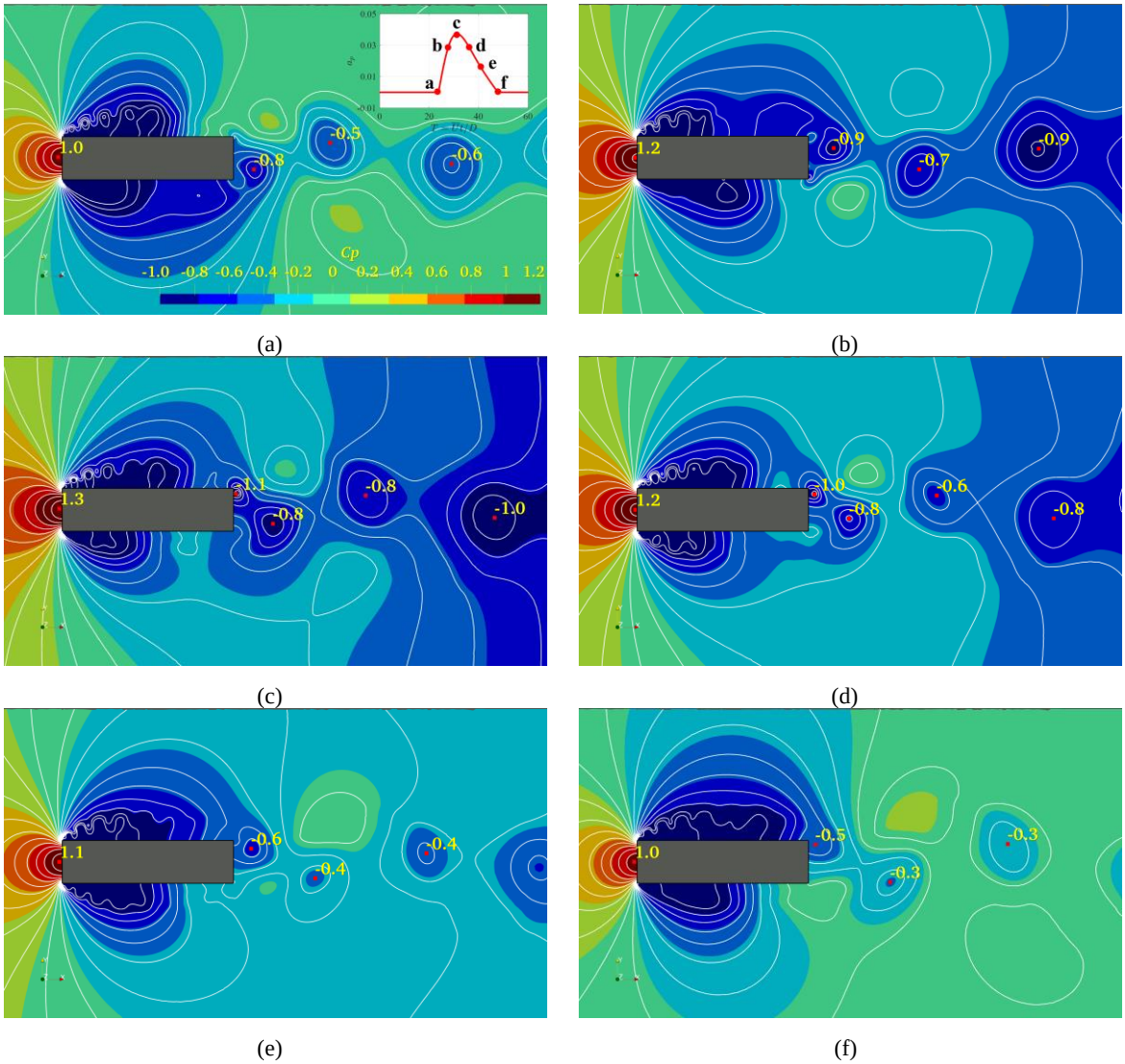

Figure 16. Pressure flow fields for *R*4 under *S*-3 conditions at different time instants: (a) *T*=24; (b) *T*=27.6864; (c) *T*=31.3752; (d) *T*=36; (e) *T*=40.8; (f) *T*=48.

Figure 17 (a) presents the time-varying lift coefficients C_L (*t*) and their respective envelope curves of *R*4 under *S*-1、*S*-2 and *S*-3 accelerating inflows. As $a_{p,max}$ increases from 0.009 to 0.036, the amplitude of C_L (*t*) decreases by approximately 17.8%, 35.2% and 59.4%, respectively, compared to the steady case. This indicates that accelerating inflows can decrease the VIV forces, which is consistent with the experimental results by [24, 25, 53]. Figure 17 (b) presents the corresponding mean and standard deviation distributions. As $a_{p,max}$ increases from 0 to 0.036, the accelerating flows have minimal effects on the mean value, but significantly

reduce the standard deviation of the pressure coefficients. Compared to the steady case, the peak value of C_p' decrease by approximately 8.8%, 17.2%, and 32.9%, respectively, leading to a reduction in the fluctuation amplitude of lift coefficients.

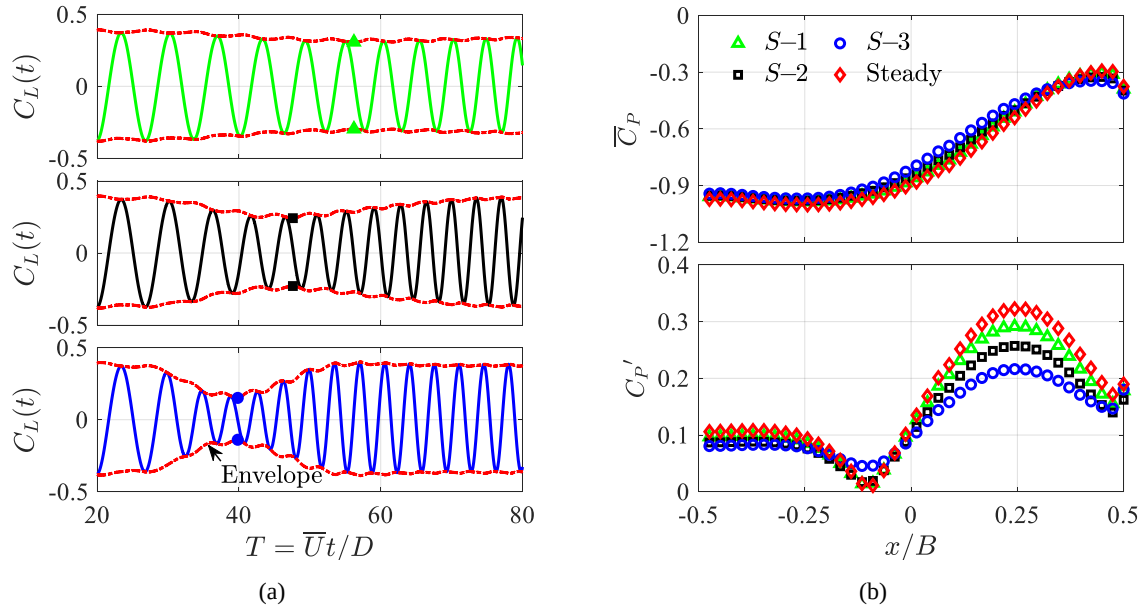

(a) (b)

Figure 17. Lift Statistics of *R*4 in different *Sinusoidal*-type inflows: (a) time history of lift coefficients; (b) mean and stand deviation of pressure distributions during acceleration.

5.3 Effects of turbulence components

In order to clarify the turbulence effect in accelerating inflows, Figure 18 presents the LES results for *R*4 under *Turbulent*-type accelerating inflows, with turbulence intensity 0%, 5%, 10% and 15%. The Morison values, calculated using Eq.(3) with the added mass coefficient C_a of 1.37 from URANS, are also compared. Significant overshoot phenomena are observed also in this case, consistently with the previously presented results. The time-varying-mean drag coefficients obtained under the four accelerating inflows with different turbulence intensities are well-described by Morison equation. This indicates that turbulence have limited effects on the drag overshoot and the Morison equation is also suitable for accelerating turbulent inflows.

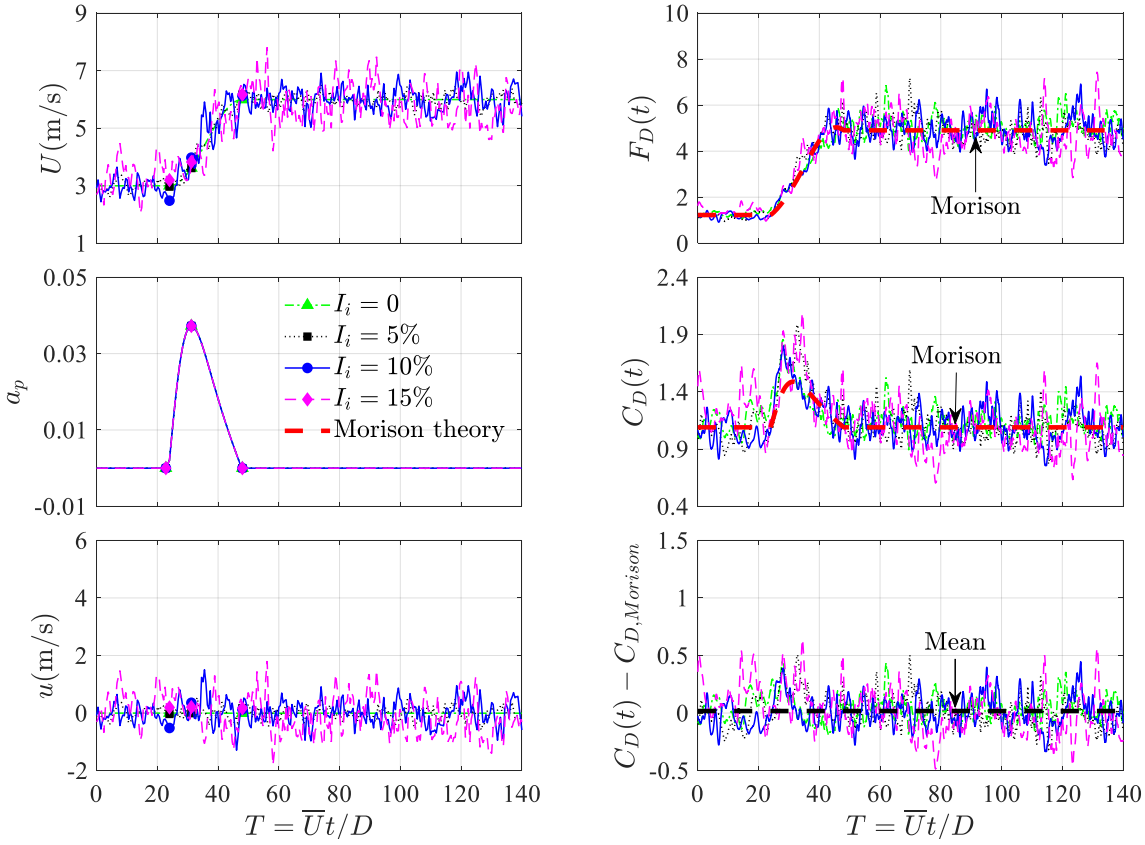

Figure 18. Drag forces of *R*4 from LES under *Turbulent*-type accelerating flows with varying turbulence intensities: (a) U and a_p; (b) $F_D(t) - \bar{F}_D$ and $C_D(t) - \bar{C}_D$.

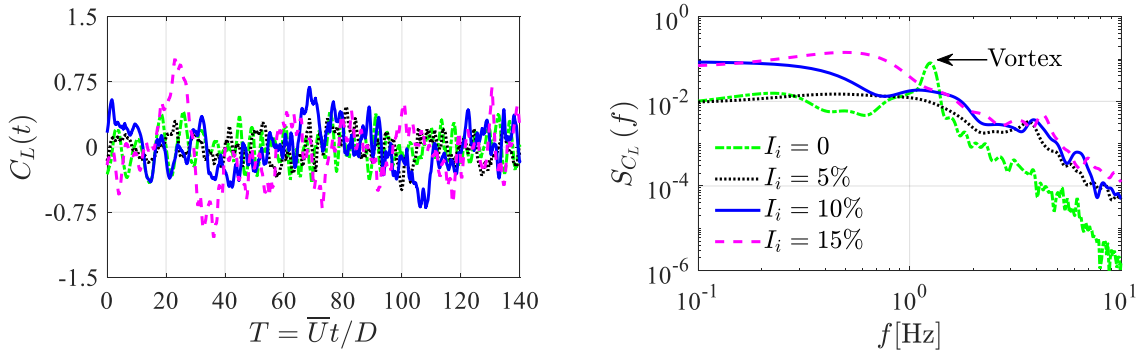

Figure 19 Lift coefficients from LES under *Turbulent*-type accelerating inflows with varying turbulence intensities: (a) time history; (b) spectrum.

Figure 19 presents the time history and spectrum of lift coefficients of *R*4 under *Turbulent*-type accelerating inflows with turbulence intensity of 0~15%. It can be found that turbulence clearly reduces the vortex induced forces, while obviously increasing buffeting forces. Figure 20 further compares the corresponding coherent structure of *R*4. Similar to URANS results, vortex shedding in accelerating inflows without turbulence is slightly weaker than in steady

cases. Once more, increasing turbulence intensity diminish the vortex shedding intensity, which is similar to its effects on the VIV in steady case [88].

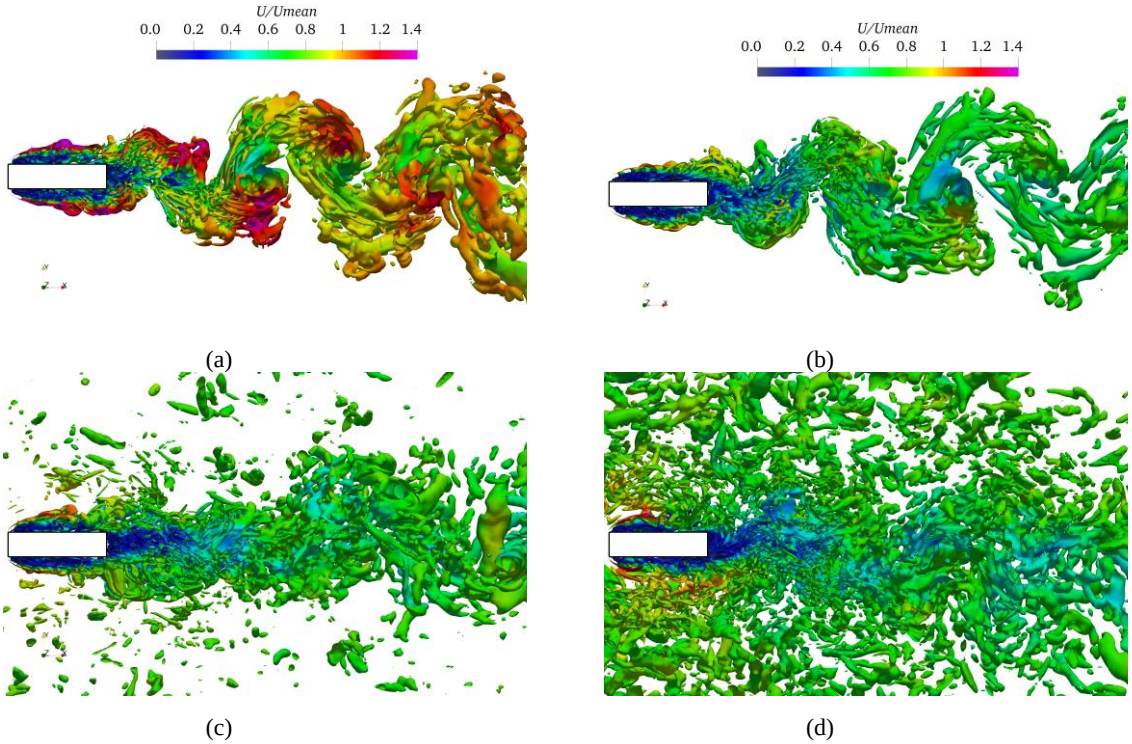

Figure 20 Q criterion of the instantous coherent structure for different turbulence intensity(Q=0.50 s^{-2}): (a) Steady flow (b) I_i=0; (c) I_i=5%; (d) I_i=10%.

5.4 Effects of aspect ratio

Next, we report the effects of the aspect ratio on the drag overshoot of rectangular cylinders. Figure 21 shows the drag coefficients for R3, R4, R5, and R8, R10, R12, R16 under the S-3 accelerating flow condition. The overshoot of drag coefficient increases rapidly with the aspect ratio. For R3, R4, and R5, the maximum drag coefficients exceed the quasi-steady values by 22.4%, 32.6%, and 46.1%, respectively, while for R8, R10, R12, and R16, the increases are 74.0%, 82.0%, 94.3%, and 109.7%, respectively. Notably, at the end of the acceleration phase (t=t_e), the drag coefficients for the investigated rectangular cylinders, except R3, do not immediately return to the quasi-steady values. For R4 and R5, they are 11.5% and 13.5% lower, while for R8, R10, R12, and R16, they are 12.0%, 14.6%, 32.9%, and 26.4% higher than the quasi-steady values, respectively.

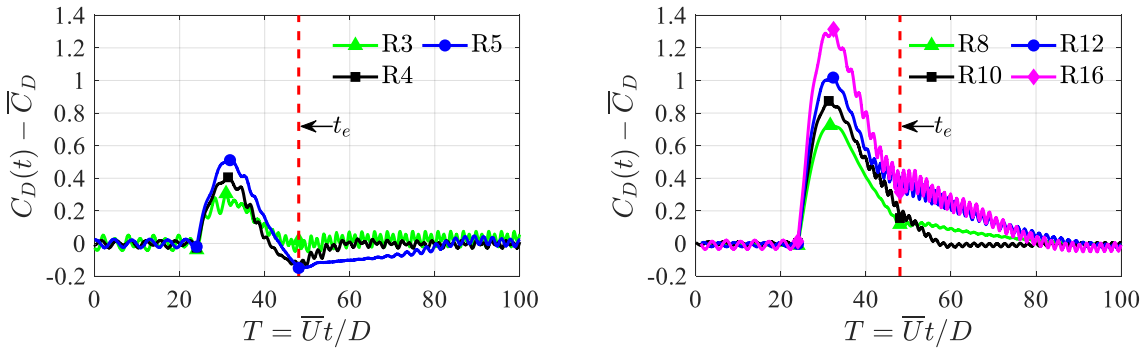

(a) (b)

Figure 21. Drag coefficients for different rectangular cylinders for *Sinusoidal*-type inflow *S*-3: (a) *R*3, *R*4, *R*5; (b) *R*8, *R*10, *R*12 and *R*12;

Figure 22 further presents drag coefficients versus the acceleration parameters a_p for rectangular cylinders under the *S*-3 accelerating inflows. The results are fitted using the Morison theory in Eq.(3). The added mass coefficients C_a for *R*3, *R*5, *R*10, and *R*16 are 1.49, 1.42, 1.18, and 1.09, respectively. During the a_p ramp-up phase, the drag coefficients closely match the Morison values. However, during the ramp-down phase, especially when a_p is between 0 to 0.01, the drag coefficients does not return to the quasi-steady state, causing deviations from Morison theory.

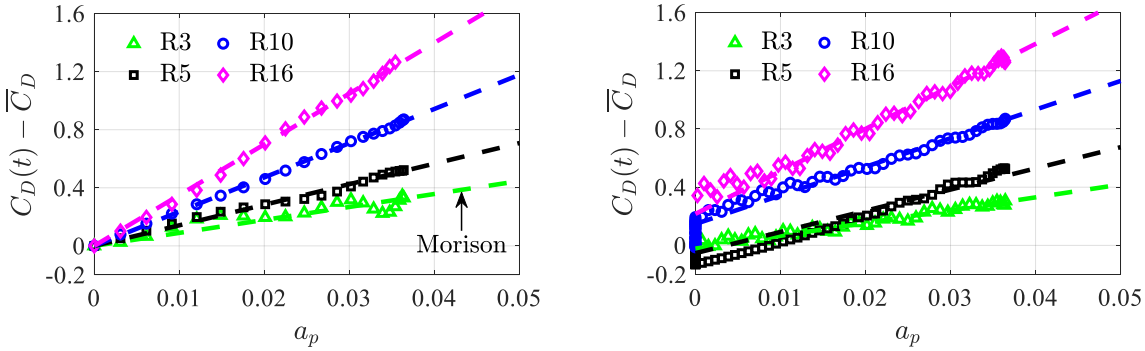

(a) (b)

Figure 22. Drag coefficients vs accelerate parameter a_p for different rectangular cylinders: (a) a_p ramp-up phase; (b) a_p ramp-down phase.

Figure 23(a) shows the added mass coefficient C_a versus the aspect ratio *R* obtained from CFD. In particular, the fitted empirical formula is given as follows:

$$C_a = aR^{-b}, \tag{12}$$

where *a*=1.90, *b*=0.20 are the empirical coefficients. Substituting Eq.(12) into Eq.(3), the drag coefficients for rectangular cylinders under accelerating inflows can be evaluated as:

$$C_D(\mathrm{t}) = \bar{C}_D + 2aR^{1-b}a_p\,. \tag{13}$$

Based on the above proposed empirical formula, Figure 23(b) shows the surface plot of drag coefficient as a function of the non-dimensional parameters a_p and aspect ratio R. The proposed formula agrees well with the CFD results, showing that the drag overshoot increases with a_p and becomes more significant as the aspect ratio increases. Notably, streamlined bridge decks with large aspect ratios are commonly used in long-span bridges. Therefore, the drag overshoot caused by accelerating flows with high a_p should be considered in their design.

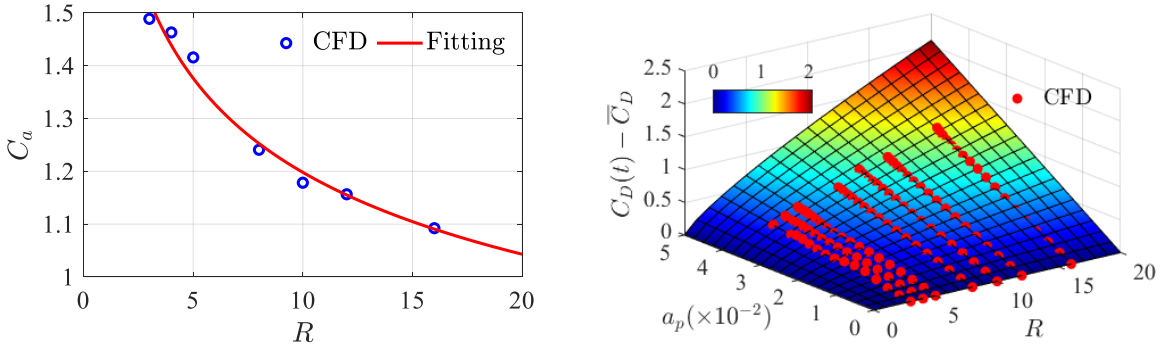

(a) (b)

Figure 23. Drag coefficients for rectangular cylinders: (a) identified added mass coefficients vs. aspect ratio; (b) empirical formula surface plot vs. a_p and aspect ratio.

Finally, Figure 24 compares the time history of drag coefficients from CFD with predictions using the proposed empirical formula in Eq.(13). The formula accurately predicts drag coefficients during the a_p ramp-up phase. However, the drag overshoot during a_p ramp-down phase depends on both a_p and the type of accelerating inflow. When a_p decrease below 0.01, the formula overestimates drag coefficients by up to 13.6% for $R3$ and $R5$, and underestimates them by up to 26.6% for $R10$ and $R16$ during the a_p ramp-down phase.

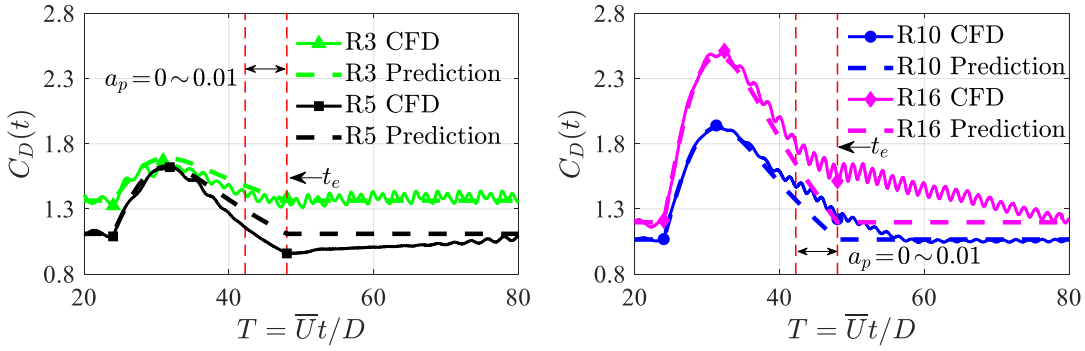

(a) (b)

Figure 24. Comparison between empirical formula predictions and CFD for the drag coefficients of rectangular cylinders: (a) $R3$ and $R5$ (b) $R10$ and $R16$

6. Conclusions

This paper employs URANS and LES to investigate the aerodynamic drag overshoot of rectangular cylinders with aspect ratios from 3 to 16 under four types of accelerating inflows. Sixteen acceleration cases, varying in acceleration start and end speeds, duration, non-dimensional parameters $a_p(D(dU/dt)/U^2)$, turbulence intensity and aspect ratio, are analyzed to identify key factors influencing aerodynamic overshoot. The accuracy of CFD simulations is confirmed by their good agreement with WTTs [22, 56] . The main conclusions are as follows:

(1) All investigated rectangular cylinders exhibit drag overshoot under accelerating inflows. According to the Morrison model, the parameter $a_p(D(dU/dt)/U^2)$, non-dimensional by instantaneous speeds, determines the overshoot. During the a_p ramp-up phase, both windward positive and leeward negative pressures increase, causing the overshoot to rise linearly with a_p. During a_p ramp-down phase, drag overshoot is not only influenced by a_p but also by acceleration duration and inflow type.

(2) The drag overshoot increases with aspect ratio. For rectangular cylinders with aspect ratios from 3 to 16 under acceleration inflows with a_p of 0.036, the drag coefficients increase by 22.4%~109.7% compared to the quasi-static case. Therefore, drag overshoot must be considered for long-span bridges with large aspect ratio decks exposed to non-synoptic winds with high a_p.

(3) No vortex-shedding induced lift coefficient overshoot is observed for investigated acceleration cases. Instead, it appears that accelerating inflows reduce fluctuating lift coefficients by lowering fluctuating pressures at the trailing edge.

(4) As the turbulence intensity of the accelerating inflows increases from 0 to 15%, the drag overshoot of rectangular cylinder with an aspect ratio 4 is substantially unaffected. Therefore, turbulence has limited effects on drag overshoot, being the main effect to reduce vortex-induced forces as in stationary cases.

(5) The proposed empirical formula based on Morison theory and identified added mass coefficients can well estimate the drag overshoot for rectangular cylinders during a_p ramp-up phase. However, for a_p ramp-down phase that involves complex overshoot, the formula

overestimates drag coefficients by approximately 13.6% for smaller aspect ratios (3 to 5) and underestimates them by about 26.6% for larger aspect ratios (10~16). Despite these discrepancies, the formula provides useful guidelines for estimating drag loads on bluff bodies in accelerating inflows.

Acknowledgments

The authors express their gratitude for financial support from National Key Research and Development Program of China (2022YFC3005302), National Natural Science Foundation of China (52408514), China Postdoctoral Science Foundation (2023M740786 & 2024T170188), Natural Science Foundation of Guangxi (2025GXNSFBA069139) and Guangxi Science and Technology Base and Talent Project (AA23026011 & AD23026185).

Data availability

The data that support the findings of this study are available from the corresponding author upon reasonable request.

Author Contributions

All authors contributed to this work.

Conflicts of Interest

The authors declare no conflict of interest.

References:

[1] H. Zhang, H. Wang, Z. Xu, Numerical study of wind loads on the streamlined bridge deck in the translating tornado-like vortex, Physics of Fluids, 35 (2023).

[2] R.-D. Xue, G. Chen, X.-H. Xiong, Aerodynamic characteristics of the train under real wind gust, Physics of Fluids, 36 (2024).

[3] P. Hu, F. Zhang, Y. Han, C. Cai, Z. Wang, J. Long, Aerodynamic characteristics of the train under the stationary thunderstorm downburst wind, Physics of Fluids, 36 (2024).

[4] T.T. Fujita, Downbursts: meteorological features and wind field characteristics, Journal of Wind Engineering and Industrial Aerodynamics, 36 (1990) 75-86.

[5] H. Wang, A. Li, J. Niu, Z. Zong, J. Li, Long-term monitoring of wind characteristics at Sutong Bridge site, Journal of Wind Engineering and Industrial Aerodynamics, 115 (2013) 39-47.

[6] H. Wang, T. Wu, T. Tao, A. Li, A. Kareem, Measurements and analysis of non-stationary wind characteristics at Sutong Bridge in Typhoon Damrey, Journal of Wind Engineering and Industrial Aerodynamics, 151 (2016) 100-106.
[7] M. Burlando, D. Romanic, G. Boni, M. Lagasio, A. Parodi, Investigation of the weather conditions during the collapse of the Morandi Bridge in Genoa on 14 August 2018 using field observations and WRF model, Atmosphere, 11 (2020) 724.
[8] Y. Feng, Q. Su, J. Hao, W. Han, H. Wang, A comparative study on the transient wind-induced response of long-span bridges subject to downbursts and typhoons, Engineering Structures, 280 (2023) 115649.
[9] X. Chen, Analysis of multimode coupled buffeting response of long-span bridges to nonstationary winds with force parameters from stationary wind, Journal of Structural Engineering, 141 (2015) 04014131.
[10] T. Tao, H. Wang, P. Shi, H. Li, Stationary and non-stationary buffeting analyses of a long-span bridge under typhoon winds, Wind and Structures, 31 (2020) 445-457.
[11] Y. Su, G. Huang, Y.-l. Xu, Derivation of time-varying mean for non-stationary downburst winds, Journal of Wind Engineering and Industrial Aerodynamics, 141 (2015) 39-48.
[12] L. Hu, Y.-L. Xu, W.-F. Huang, Typhoon-induced non-stationary buffeting response of long-span bridges in complex terrain, Engineering Structures, 57 (2013) 406-415.
[13] Z. Xu, G. Dai, L. Zhang, Y.F. Chen, R.G. Flay, H. Rao, Effect of non-Gaussian turbulence on extreme buffeting response of a high-speed railway sea-crossing bridge, Journal of Wind Engineering and Industrial Aerodynamics, 224 (2022) 104981.
[14] T. Sarpkaya, C. Ihrig, Impulsively started steady flow about rectangular prisms: experiments and discrete vortex analysis, Journal of Fluids Engineering, DOI (1986).
[15] T. Sarpkaya, H. Kline, Impulsively-started flow about four types of bluff body, Journal of Fluids Engineering, DOI (1982).
[16] T. Sarpkaya, Separated flow about lifting bodies and impulsive flow about cylinders, AIAA Journal, 4 (1966) 414-420.
[17] T. Sarpkaya, Lift, drag, and added-mass coefficients for a circular cylinder immersed in a time-dependent flow, Journal of Applied Mechanics, 30 (1963) 13-15.
[18] T. Takeuchi, J. Maeda, Unsteady wind force on an elliptic cylinder subjected to a short-rise-time gust from steady flow, Journal of Wind Engineering and Industrial Aerodynamics, 122 (2013) 138-145.
[19] X. Dong, L. Zhao, W. Cui, Y. Peng, Y. Ge, Aerodynamics and aeroelastic performance of a rigid-frame bridge with a bluff body girder subjected to short-rise-time gusts, Engineering Structures, 263 (2022) 114376.
[20] B. Yan, Y. Yuan, X. Zhou, Y. Li, Q. Yang, Q. Liu, W. Yang, J. Han, Experimental study of non-stationary aerodynamic effects on the wind turbine nacelles under extreme wind events, Physics of Fluids, 36 (2024).
[21] S. Li, X. Li, Y. Jiang, T. Li, Y. Wang, Non-stationary aerodynamic characteristics of the rectangular cylinder in downburst-like flow, Physics of Fluids, 37 (2025).
[22] T. Yang, M.S. Mason, Aerodynamic characteristics of rectangular cylinders in steady and accelerating wind flow, Journal of Fluids and Structures, 90 (2019) 246-262.
[23] V. Le, L. Caracoglia, Experimental investigation on non-stationary wind loading effects generated with a multi-blade flow device, Journal of Fluids and Structures, 96 (2020) 103049.
[24] S. Brusco, H.-Y. Bin, Y.-L. Lo, G. Piccardo, Transient aerodynamics of a square cylinder under downburst-like accelerating flows reproduced in a multiple-fan wind tunnel, Journal of Fluids and Structures, 124 (2024) 104038.

[25] X.-Y. Chen, L.-D. Zhu, Z.-X. Tan, Experimental investigation on key parameters influencing unsteady aerodynamics of a 3: 2 rectangular prism in accelerating flow, Physics of Fluids, 36 (2024).
[26] T. Takeuchi, J. Maeda, Overshoot of wind forces on a body under step-function-like gusty winds, Journal of Structural and Construction Engineering: Transactions of AIJ, 681 (2012) 1629-1635.
[27] S. Zhang, Q. Yang, G. Solari, B. Li, G. Huang, Characteristics of thunderstorm outflows in Beijing urban area, Journal of Wind Engineering and Industrial Aerodynamics, 195 (2019) 104011.
[28] S. Zhao, Y. Ge, G. Kopp, Assessment of gust factors and wind speed decomposition methods for thunderstorms, Journal of Wind Engineering and Industrial Aerodynamics, 223 (2022) 104953.
[29] K. Cai, M. Huang, Y. Dong, S. Liao, Y.-Q. Ni, P. Chan, Nonstationary Turbulent Wind Speed Models and Their Effects on Wind-Induced Responses of Tall Buildings, Journal of Structural Engineering, 151 (2025) 04025003.
[30] F. Jiang, M. Zhang, Y. Li, T. Yan, J. Zhang, Field measurement analysis of wind parameters and nonstationary characteristics in mountainous terrain: focusing on cooling windstorms, Journal of Wind Engineering and Industrial Aerodynamics, 230 (2022) 105175.
[31] M. Chay, C. Letchford, Pressure distributions on a cube in a simulated thunderstorm downburst—Part A: stationary downburst observations, Journal of Wind Engineering and Industrial Aerodynamics, 90 (2002) 711-732.
[32] D. Romanic, A. Kassab, J. Chowdhury, H. Hangan, L. Doddipatla, An analysis of the influence of a generic building on tornadic flow fields using high-frequency PIV and point velocity measurements, Journal of Fluids and Structures, 123 (2023) 104010.
[33] J. Žužul, A. Ricci, M. Burlando, B. Blocken, G. Solari, CFD analysis of the WindEEE dome produced downburst-like winds, Journal of Wind Engineering and Industrial Aerodynamics, 232 (2023) 105268.
[34] F. Canepa, M. Burlando, D. Romanic, G. Solari, H. Hangan, Downburst-like experimental impinging jet measurements at the WindEEE Dome, Scientific Data, 9 (2022) 243.
[35] S. Brusco, G. Buresti, Y.-L. Lo, G. Piccardo, I. Aerodynamics, Constant-frequency time cells in the vortex-shedding from a square cylinder in accelerating flows, Journal of Wind Engineering, 230 (2022) 105182.
[36] X. Li, S. Li, Q. Yang, Y. Hui, S. Cao, Time-varying up-crossing theory-based non-stationary extreme estimation of gust-loading on rectangular cylinder due to thunderstorm-like wind, Probabilistic Engineering Mechanics, 74 (2023) 103506.
[37] Y. Yuan, B. Yan, X. Zhou, X. Li, Y. Dong, Q. Yang, Q. Liu, Evolution of downburst-like flows produced by an active-controlled multi-blade facility, Physics of Fluids, 36 (2024).
[38] S. Zou, X. He, Generation of a mountain-valley wind in an atmospheric boundary wind tunnel: a gust-wind generator study, Advances in Bridge Engineering, 4 (2023) 4.
[39] N.D. Tiwari, P.P. Sarkar, Prediction of dynamic loads and responses of a tall building in tornado wind: Numerical analysis and experimental validation, Engineering Structures, 326 (2025) 119510.
[40] L. Zhao, L. Zhang, W. Cui, S. Cao, Y. Ge, The reproduction of 2-D non-synoptic wind field in an actively controlled wind tunnel, Journal of Wind Engineering and Industrial Aerodynamics, 251 (2024) 105786.
[41] T. Ghazal, M. Aboutabikh, H. Aboshosha, M. Abdelwahab, Thunderstorm wind load evaluation on storm shelters using wind tunnel testing, Engineering Structures, 262 (2022) 114350.
[42] E.-S. Abd-Elaal, J.E. Mills, X. Ma, A coupled parametric-CFD study for determining ages of downbursts through investigation of different field parameters, Journal of Wind Engineering and Industrial Aerodynamics, 123 (2013) 30-42.

[43] C. Li, Q. Li, Y. Xiao, J. Ou, A revised empirical model and CFD simulations for 3D axisymmetric steady-state flows of downbursts and impinging jets, Journal of Wind Engineering and Industrial Aerodynamics, 102 (2012) 48-60.
[44] M. Haines, I. Taylor, Numerical investigation of the flow field around low rise buildings due to a downburst event using large eddy simulation, Journal of Wind Engineering and Industrial Aerodynamics, 172 (2018) 12-30.
[45] L. Patruno, M. Ricci, A systematic approach to the generation of synthetic turbulence using spectral methods, Computer methods in applied mechanics and engineering, 340 (2018) 881-904.
[46] T. Ma, C. Sun, P. Miller, Large eddy simulation of non-stationary highly turbulent hurricane boundary layer winds, Physics of Fluids, 36 (2024).
[47] Z. Fang, Z. Wang, H. Huang, L. Yang, Y. Guo, Numerical simulations of downburst wind fields: A comparative analysis of stationary and moving storms using the impinging jet model, Physics of Fluids, 36 (2024).
[48] P. Hu, Y. Tang, Y. Han, C. Cai, N. Yan, F. Zhang, Numerical study on self-excited forces and flow fields for a thin plate under a sinusoidal non-stationary wind condition, Physics of Fluids, 35 (2023).
[49] Y. Pan, M. Liu, C. Zhang, Z. Xie, Temporal variability wind characterization analysis and model construction of moving downbursts, Physics of Fluids, 37 (2025).
[50] W. Li, L. Patruno, H. Niu, S. de Miranda, X. Hua, Aerodynamic admittance of a 6: 1 rectangular cylinder: A computational study on the role of turbulence intensity and integral length scale, Journal of Wind Engineering and Industrial Aerodynamics, 218 (2021) 104738.
[51] Y. Zhang, S. Cao, J. Cao, J. Wang, Effects of turbulence intensity and integral length scale on the surface pressure on a rectangular 5: 1 cylinder, Journal of Wind Engineering and Industrial Aerodynamics, 236 (2023) 105406.
[52] F. Guo, G. Wu, X. Du, M.S. Mason, Numerical investigation of flow around a square cylinder in accelerated flow, Physics of Fluids, 33 (2021).
[53] G. Lunghi, S. Brusco, A. Mariotti, G. Piccardo, M. Salvetti, Influence of inflow acceleration on the aerodynamic characteristics of a square cylinder, Journal of Wind Engineering and Industrial Aerodynamics, 252 (2024) 105814.
[54] T. Takeuchi, N. Takeuchi, J. Maeda, Y.C. Kim, Characteristics of local wind force and wind response of a building under short-rise-time gusts, 9th Asia-Pacific Conference on Wind Engineering, 2017.
[55] J. Xing, L. Patruno, S. de Miranda, F. Ubertini, Non-stationary winds effects over large partially-open roofs: A CFD study regarding the role of unsteady aerodynamics, Structures, 65 (2024) 106728.
[56] Y. Xiao, Aerodynamic Characteristics of 5:1 Rectangular Cylinder Subjected to Transient Flow, Southwest Jiaotong University, 2022.
[57] S. Brusco, G. Buresti, G. Piccardo, Thunderstorm-induced mean wind velocities and accelerations through the continuous wavelet transform, Journal of Wind Engineering and Industrial Aerodynamics, 221 (2022) 104886.
[58] J. Morison, J.W. Johnson, M. O'Brien, Experimental studies of forces on piles, Coastal Engineering Proceedings, DOI (1953) 25-25.
[59] J.R. Morison, J.W. Johnson, S.A. Schaaf, The force exerted by surface waves on piles, Journal of Petroleum Technology, 2 (1950) 149-154.
[60] C. Clément, P. Bozonnet, G. Vinay, P. Pagnier, A.B. Nadal, J. Réveillon, Evaluation of Morison approach with CFD modelling on a surface-piercing cylinder towards the investigation of FOWT Hydrodynamics, Ocean Engineering, 251 (2022) 111042.

[61] K. Xu, Y. Shao, Z. Gao, T. Moan, A study on fully nonlinear wave load effects on floating wind turbine, Journal of Fluids and Structures, 88 (2019) 216-240.
[62] R.H. Kraichnan, Diffusion by a random velocity field, Physics of Fluids, 13 (1970) 22-31.
[63] S. Li, R. Snaiki, T. Wu, Active simulation of transient wind field in a multiple-fan wind tunnel via deep reinforcement learning, Journal of Engineering Mechanics, 147 (2021) 04021056.
[64] K. Butler, S. Cao, A. Kareem, Y. Tamura, S. Ozono, Surface pressure and wind load characteristics on prisms immersed in a simulated transient gust front flow field, Journal of Wind Engineering and Industrial Aerodynamics, 98 (2010) 299-316.
[65] Z. Li, T. Chan, J. Ko, Evaluation of typhoon induced fatigue damage for Tsing Ma Bridge, Engineering Structures, 24 (2002) 1035-1047.
[66] H. Wang, T. Tao, Y. Gao, F. Xu, Measurement of wind effects on a kilometer-level cable-stayed bridge during Typhoon Haikui, Journal of Structural Engineering, 144 (2018) 04018142.
[67] X. Wang, H. Li, Z. Chen, Y. Qian, Y. Wang, X. Peng, Field measurement of near-surface typhoon characteristics using a smart monitoring system on a long-span arch bridge site, Advances in Structural Engineering, 22 (2019) 1977-1987.
[68] M. Mason, T. Yang, Unsteady pressures on a square cylinder subjected to transient wind fields, 12th UK Conference on Wind Engineering, 2016.
[69] F. Nieto, D. Hargreaves, J. Owen, S. Hernández, On the applicability of 2D URANS and SST k-ω turbulence model to the fluid-structure interaction of rectangular cylinders, Engineering Applications of Computational Fluid Mechanics, 9 (2015) 157-173.
[70] A. Álvarez, F. Nieto, K. Kwok, S. Hernández, Aerodynamic performance of twin-box decks: A parametric study on gap width effects based on validated 2D URANS simulations, Journal of Wind Engineering and Industrial Aerodynamics, 182 (2018) 202-221.
[71] W. Li, L. Patruno, H. Niu, S. de Miranda, X. Hua, Identification of complex admittance functions using 2D-URANS models: Inflow generation and validation on rectangular cylinders, Journal of Wind Engineering and Industrial Aerodynamics, 208 (2021) 104435.
[72] A. Álvarez, F. Nieto, D. Nguyen, J. Owen, S. Hernández, 3D LES simulations of a static and vertically free-to-oscillate 4: 1 rectangular cylinder: Effects of the grid resolution, Journal of Wind Engineering and Industrial Aerodynamics, 192 (2019) 31-44.
[73] D.T. Nguyen, D.M. Hargreaves, J.S. Owen, Vortex-induced vibration of a 5: 1 rectangular cylinder: A comparison of wind tunnel sectional model tests and computational simulations, Journal of Wind Engineering and Industrial Aerodynamics, 175 (2018) 1-16.
[74] L. Bruno, M.V. Salvetti, F. Ricciardelli, Benchmark on the aerodynamics of a rectangular 5: 1 cylinder: an overview after the first four years of activity, Journal of Wind Engineering and Industrial Aerodynamics, 126 (2014) 87-106.
[75] P. Zou, S. Cao, J. Cao, Spanwise correlation and coherent structures of separated flow around rectangular 5: 1 cylinder, Journal of Wind Engineering and Industrial Aerodynamics, 231 (2022) 105211.
[76] Z. Zhang, F. Xu, Spanwise length and mesh resolution effects on simulated flow around a 5: 1 rectangular cylinder, Journal of Wind Engineering and Industrial Aerodynamics, 202 (2020) 104186.
[77] T. Igarashi, Characteristics of the flow around rectangular cylinders: the case of the angle of attack 0 deg, Bulletin of JSME, 28 (1985) 1690-1696.

[78] H. Noda, A. Nakayama, Free-stream turbulence effects on the instantaneous pressure and forces on cylinders of rectangular cross section, Experiments in fluids, 34 (2003) 332-344.
[79] C. Norberg, Flow around rectangular cylinders: pressure forces and wake frequencies, Journal of Wind Engineering and Industrial Aerodynamics, 49 (1993) 187-196.
[80] L. Thiesemann, Zur Ermittlung von Flatterderivativa aus Versuchen und mittels numerischer Strömungsmechanik, Shaker2008.
[81] X. Amandolese, Contribution à l'étude des chargements fluides sur des obstacles non profilés fixes ou mobiles: application aux tabliers de pont, Marne-la-Vallée, ENPC, 2001.
[82] G. Schewe, Reynolds-number-effects in flow around a rectangular cylinder with aspect ratio 1: 5, Journal of Fluids and Structures, 39 (2013) 15-26.
[83] C. Mannini, A.M. Marra, L. Pigolotti, G. Bartoli, The effects of free-stream turbulence and angle of attack on the aerodynamics of a cylinder with rectangular 5: 1 cross section, Journal of Wind Engineering and Industrial Aerodynamics, 161 (2017) 42-58.
[84] B. Wu, S. Li, S. Cao, Q. Yang, L. Zhang, Numerical investigation of the separated and reattaching flow over a 5: 1 rectangular cylinder in streamwise sinusoidal flow, Journal of Wind Engineering and Industrial Aerodynamics, 198 (2020) 104120.
[85] M. Li, Q. Li, H. Shi, Aerodynamic pressures on a 5: 1 rectangular cylinder in sinusoidal streamwise oscillatory flows with non-zero mean velocities, Journal of Wind Engineering and Industrial Aerodynamics, 208 (2021) 104440.
[86] L. Patruno, M. Ricci, S. de Miranda, F. Ubertini, Numerical simulation of a 5: 1 rectangular cylinder at non-null angles of attack, Journal of Wind Engineering and Industrial Aerodynamics, 151 (2016) 146-157.
[87] S. de Miranda, L. Patruno, F. Ubertini, G. Vairo, On the identification of flutter derivatives of bridge decks via RANS turbulence models: Benchmarking on rectangular prisms, Engineering Structures, 76 (2014) 359-370.
[88] S.J. Daniels, I.P. Castro, Z.-T. Xie, Numerical analysis of freestream turbulence effects on the vortex-induced vibrations of a rectangular cylinder, Journal of Wind Engineering and Industrial Aerodynamics, 153 (2016) 13-25.